

# An Atlas of H $\alpha$ and R Images and Radial Profiles of 63 Bright Virgo Cluster Spiral Galaxies

Rebecca A. Koopmann

*Union College*

*Department of Physics, Schenectady, NY 12308*

`koopmanr@union.edu`

Jeffrey D. P. Kenney

*Astronomy Department*

*Yale University, P.O. Box 208101, New Haven, CT 06520-8101*

`kenney@astro.yale.edu`

Judith Young

*University of Massachusetts*

*Five Colleges Radio Observatory*

*6191 Graduate Res. Ctr., Amherst, MA, 01003*

`young@phast.umass.edu`

## ABSTRACT

Narrow-band H $\alpha$  and broadband R images and radial profiles are presented for 63 bright spiral galaxies in the Virgo Cluster. The sample is complete for Sb-Scd galaxies with  $B_T^0 \leq 12$  and inclination  $\leq 75^\circ$ . Isophotal radii, disk scalelengths, concentration parameters, and integrated fluxes are derived for the sample galaxies.

*Subject headings:* galaxies: spiral, galaxies: star formation, galaxies: clusters: general, galaxies: clusters: individual name: Virgo, galaxies: fundamental parameters, galaxies: peculiar, galaxies: structure

## 1. Introduction

How has the environment affected the star formation properties of spiral galaxies in clusters? Previous measurements of the global star formation rates at H $\alpha$ , UV, and far-infrared wavelengths of cluster spirals show that some cluster spirals have reduced global star formation (Kennicutt 1983, Bica & Giovanelli 1987, Kodaira et al. 1990, Moss & Whittle 1993), others have similar global star formation rates (Kennicutt, Bothun, & Schommer 1984, Gavazzi et al. 1991, Donas et al. 1990), and some have enhanced star formation rates (Moss & Whittle 1993, Bennett & Moss 1998) with respect to field counterparts.

Studies of the spatial distributions of star formation have been more limited and have usually concentrated on field spiral samples (e.g., Hodge & Kennicutt 1983; Ryder & Dopita 1993; Phillips 1993; González Delgado et al. 1997; Hameed & Devereux 1999). Based on these studies, star formation tends to be distributed over much of the optical disk, often concentrated along spiral arms and in rings. To date there has been little comparison of high resolution spatial distributions of star formation for large samples of cluster and field galaxies. Such comparisons could help reveal where in the disk star formation has been reduced or enhanced in cluster galaxies, leading to strong constraints on the environmental mech-

anisms which transform cluster galaxies.

The R and H $\alpha$  images presented in this paper are part of an extensive study of the spatial distributions of massive star formation in nearly 100 Virgo Cluster and isolated spiral and lenticular galaxies. The main goal of the work is to better understand the relative distributions of star formation in cluster and isolated spirals and to probe the role of the environment in the star formation properties of cluster spirals.

The sample presented in this paper is drawn from the nearby Virgo Cluster of galaxies. The Virgo Cluster is an excellent laboratory for studies of star formation histories since it is near enough that galaxy morphology can be examined in detail. It has also been surveyed at many different wavelengths, including aperture H $\alpha$  (Kennicutt 1983), HI (Warmels 1988, Cayatte et al. 1990, Hoffman et al. 1989), CO (Kenney & Young 1989), near-IR (Boselli et al. 1997), radio continuum (Kotanyi 1980) and X-ray (Boehringer et al. 1994). The structure and membership of the cluster are well-studied (Binggeli, Sandage, & Tammann 1985; Binggeli, Tammann, & Sandage 1987; Binggeli, Popescu, & Tammann 1993; Yasuda, Fukugita, & Okamura 1997; Gavazzi et al. 1999, Schindler, Binggeli, & Boehringer 1999). Because the cluster has not yet relaxed, there is an enhanced likelihood of detecting ongoing environmental alteration.

This paper presents continuum-subtracted H $\alpha$ + [N II] and broadband R images of 63 bright spiral galaxies in the Virgo Cluster. R and H $\alpha$  profiles are derived from surface photometry of the images. Isophotal radii, disk scalelengths, integrated fluxes, and concentration parameters are measured from the radial profiles. Total H $\alpha$  fluxes derived from 50 of the images presented here have already been published in Young et al. (1996), although the calibration has been adjusted in this paper.

This study marks the first presentation of H $\alpha$  spatial distributions for a large and highly complete sample of Virgo Cluster spirals. (Previous results based on H $\alpha$  images and surface brightnesses for several Virgo Cluster spirals are found in Kennicutt 1989) In addition, this study presents R surface photometry, which has been relatively rare for Virgo Cluster spirals. (Some R surface photometry is available for several galaxies within large surveys, e.g., de Jong & van der Kruit 1994).

In fact, even total R magnitudes have previously been published for only about half of this sample (Pierce & Tully 1988; Schroeder & Visvanathan 1996).

This paper is part of a series. Images and radial profiles of 30 isolated spiral galaxies are presented in Koopmann & Kenney (2001a). Concentration parameters derived from the R radial profiles and H $\alpha$  fluxes normalized by the R fluxes are used in Koopmann & Kenney (1998) to show that the Hubble classification scheme is inadequate in describing the morphology of at least 25% of Virgo Cluster spirals. The radial distributions of R and H $\alpha$  light of the Virgo Cluster and isolated galaxies are analyzed and compared in Koopmann & Kenney (2001b).

The selection of the Virgo cluster galaxies is described in Section 2. Sections 3 and 4 describe the observations and reduction procedures. The images and derived radial profiles are presented in Section 5. Surface photometry procedures are outlined in Section 6.

## 2. Sample Selection

### 2.1. Structure of the Virgo Cluster

Studies of the substructure of the Virgo Cluster (including Tully & Shaya 1984; Pierce & Tully 1988; Binggeli et al. 1987, 1993; Yasuda et al. 1997; and Gavazzi et al. 1999, Schindler et al. 1999) agree that the Virgo Cluster is made up of several associated clouds or groups of galaxies, with two main components: cluster A, associated with M87, and cluster B, associated with M49 (although Gavazzi et al. 1999 place M49 closer than cluster B, based on Tully-Fisher distances). Within subcluster A is a smaller core of mostly spheroidal galaxies. Even this core is not in dynamical equilibrium (Binggeli et al. 1987, 1993), indicating the dynamical youth of the cluster. The rest of the cluster has a filamentary structure, some of which is extended at least partially along the line of sight. One filament is the Southern Extension region of the cluster, which is a cloud of galaxies located adjacent to and at about the same distance as the central components (Binggeli et al. 1993). Three clouds of galaxies, the W (de Vaucouleurs 1961), W', and M (Ftaclas et al. 1984) clouds, are projected on the cluster; studies consistently place these clouds in the near-background

at about two times the distance of the cluster.

Membership information from the Virgo Cluster Catalog (Binggeli et al. 1985; hereafter BST) was considered in the selection of sample galaxies. Figure 1 shows a map of the locations of sample galaxies, with the projected regions of different clouds indicated. Sample galaxies are located throughout the cluster, with a range of 1-10° projected distance from M87. Possible members of the W, W', and M clouds were avoided; however the data of Binggeli et al. (1993) suggest that 4 galaxies in our sample may be located in these clouds (NGC 4189, NGC 4303, NGC 4527, and NGC 4536). Several galaxies may be members of the Southern Extension (including NGC 4457 and NGC 4586). Eight galaxies which lie outside of the limited survey region of BST were also observed (NGC 4064, NGC 4561, NGC 4643, NGC 4651, NGC 4710, NGC 4713, NGC 4772, NGC 4808); Tully-Fisher distance estimates for many of these galaxies indicate a distance consistent with the Virgo Cluster (Kenney 1987, Rubin et al. 1999).

We assume a distance of 16 Mpc for the Virgo Cluster (Jacoby et al. 1992; Yasuda et al. 1997; Kelson et al. 2000). Most of our analyses were designed to be distance-independent, since we will compare to a sample of isolated galaxies of different distances. Hence the possibility of a significant depth of the Virgo Cluster will not influence most of our conclusions.

## 2.2. Properties of Sample Galaxies

The Virgo Cluster sample galaxies range in type from S0-Sm. The galaxies were chosen to have  $B_T^0$  brighter than 13.5 (corresponding to  $M_B$  of -17.5 at an assumed distance of 16 Mpc) and inclinations mostly  $< 75^\circ$ . Seven of the 63 galaxies have higher inclination; some of these were observed in the same field of view as target galaxies. Observations of 50 of the galaxies were obtained as part of a study of star formation rates and efficiencies in 120 spiral galaxies (Young et al. 1996). This study had as selection criteria IRAS flux cutoffs of  $S_{60} > 5$  Jy or  $S_{100} > 10$  Jy. Thirteen additional galaxies, mostly of cataloged Hubble type S0-Sa, were observed as part of the current study and were not constrained by the IRAS flux criteria.

The properties of the galaxies observed are listed in Table 1. Due to the uncertain nature of

some Virgo cluster morphological classifications, Table 1 provides Hubble types from two major classifiers. Classifications were taken from the Revised Shapley-Ames Catalog of Bright Galaxies (Sandage & Tamann 1987, hereafter RSA), BST, and the Third Reference Catalog of Bright Galaxies (deVaucouleurs et al. 1991; hereafter RC3). Note that several galaxies have mixed classifications like Sc/Sa and that there are disagreements between the two major classifiers for a number of galaxies. The important issue of morphological classification is addressed further in Koopmann & Kenney (1998, 2001b).

55 out of 63 galaxies are located within the region of the Virgo Cluster surveyed by BST. The completeness values for 46 galaxies within the BST limits with  $B_T^0 < 13$  and inclination  $< 75^\circ$  are presented in Table 2 for different Hubble types. For simplicity, Hubble types were taken at face value from BST and include all peculiar types. Three galaxies with Sc/Sa or Sc/S0 classifications were counted as Sc galaxies. (We describe the morphologies of these galaxies and analyze their properties separately in other papers in this series.) Seven of the sample galaxies within the BST limits have inclinations  $\geq 75^\circ$  and 2 Sc galaxies have  $B_T^0$  between 13 and 13.5. Except for one Sa galaxy, the Virgo sample within the BST survey region is complete to  $B_T^0 < 12$  for types Sa-Sm.

## 3. Observations

Observations of sample galaxies were obtained at the KPNO (#1) 0.9-m, the CTIO 0.9-m, and the 3.5-m WIYN telescopes between March 1987 and February 1997. All observations were calibrated under photometric conditions. Exposure times ranged from 3-15 min in an R filter (nearly Mould or standard Harris/Kron-Cousins R), and 1-2 hrs in an H $\alpha$  filter of width 60-80 Å, centered either near 6563 Å or near 6600 Å (for galaxies with  $v > 1000$  km/s).

The observations of the Virgo sample galaxies were made through several different red filters. Between 1992 and 1997, images were obtained using a standard Harris (Kron-Cousins) R filter ( $\lambda = 6425$  Å,  $\Delta\lambda = 1500$  Å). Images obtained earlier were observed in either a nearly-Mould R filter ( $\lambda = 6470$  Å,  $\Delta\lambda = 1110$  Å) or, for 12% of the sample, a narrow red filter ( $\lambda = 7024$  Å,  $\Delta\lambda = 380$

Å). Filter curves are shown in Figure 2.

In order to compare these observations to an isolated comparison sample, observations in nearly Mould R were transformed to Harris R (see Section 4.2.1), using observations of Landolt standard stars in both filters. Galaxies observed in the narrow red filter were reobserved in Harris R in February 1997 at WIYN and the CTIO 0.9-m telescopes.

An observing log for the galaxies is presented in Table 3. Galaxies are listed in order of NGC/IC number, with two to three lines describing the R and H $\alpha$  observations.

A number of CCD chips were used over the course of the observations. Details of the chips are listed in Tables 3 and 4. Characteristics of the filters used in the observations are given in Table 5. The fields-of-view of the observations were large enough to image each galaxy to at least an isophotal radius of 24 mag arcsec<sup>-2</sup> and, in most cases, sufficient blank sky to accurately estimate the sky background of the chip. R observations of several of the larger Virgo galaxies obtained in the late 1980's were repeated with larger format CCD's in the 1990's to obtain a larger field-of-view.

Observations of the spectrophotometric standard stars from the lists of Massey et al. (1988) and Hamuy et al. (1992) were made for the calibration to absolute flux. Most observations obtained between 1992 and 1997 included exposures of Landolt standards (1992a) to derive the extinction coefficient.

## 4. Reduction Procedures

### 4.1. Processing

All images were bias-subtracted and flat-fielded using 5-10 dome-flats and/or twilight sky flats. For images taken at the CTIO 0.9-m, illumination corrections derived from twilight sky flats applied to the dome-flattened images significantly improved the flatness of the R sky background (from  $\sim$  2-3% to  $<$ 1%). Standard IRAF (Tody 1993) tasks were used for the processing steps.

For some galaxies, 2-3 exposures were obtained. The images were registered and aligned using the centroids of bright stars, and averaged using the *combine* task in IRAF, with cosmic ray rejection based on the noise parameters of the CCD. In the case of seeing differences, images were convolved

with a Gaussian function to the worst seeing before combining. For these images and single exposure images, the *bclean* task in the software package FIGARO and the *imedit* task in IRAF were used to remove cosmic rays.

### 4.2. Absolute Flux Calibration

Extinction coefficients were derived from exposures of Landolt standards where possible. Otherwise the standard extinction curve at KPNO or CTIO was used. Most of the R and all the H $\alpha$  images were flux calibrated based on spectrophotometric standard stars (Massey et al. 1988, Hamuy et al. 1992).

For most of the observations, the filter response curve was convolved with the spectrum of the standard to compute the expected flux within the filter. This approach is especially important for flux calibration of images in the Harris R filter. The H $\alpha$  calibrations prior to 1992 were made by approximating the total flux expected in the filter by integrating the magnitude of the standard at the central wavelength of the filter over the filter band width. This approximation has an accuracy on the order of 1-2% for the narrow-band H $\alpha$  filter, well below the error contributed from other sources. This approximation is not appropriate for the broadband R filters, particularly the Harris R filter, due to its complex transmission curve.

#### 4.2.1. Reducing to a Standard System: R

Because we wish to compare R profiles, fluxes, and size scales within the Virgo sample and to the comparison isolated sample (Koopmann & Kenney 2001a), standardization to the Harris R system is necessary. Galaxies observed in nearly Mould R were transformed to Harris R. Because no transformation equation was available in the literature, one was derived through observations of a series of Landolt (1992a) standard stars in both filters. The transformation was well described by a simple multiplicative factor, with no color dependence:

$$\frac{F_R}{F_{mR}} = 1.35 \pm 0.05$$

where  $F_R$  is the flux in R and  $F_{nmR}$  is the flux in the nearly Mould R filter. However, the scatter in the multiplicative factor introduces an additional

4% error in the R fluxes of galaxies observed in the nearly Mould R filter.

All quantities derived from the R photometry presented in this and succeeding papers are calibrated to the Harris R system. R flux values can be converted to R magnitudes using a zero point of 13.945, which was derived from comparison of spectrophotometric standard star absolute fluxes and magnitudes listed by Landolt (1992b). This relationship was also used to flux calibrate two R images for which spectrophotometric standards were not available.

There are few previous measurements of R surface photometry for Virgo Cluster galaxies. Total R magnitudes are presented by Pierce and Tully (1988) for 22 galaxies in our sample, and by Schroeder & Visvanathan (1996) for 33 galaxies in our sample. We find a correlation between the total R magnitudes and our isophotal (to 24 R mag arcsec<sup>-2</sup>) magnitudes for both sets of data, as shown in Figure 3. The Pierce & Tully magnitudes are 0.25 magnitude higher in the median than our isophotal magnitudes, with a 5% uncertainty in the slope of a linear correlation. The Schroeder & Visvanathan magnitudes are 0.11 magnitude higher in the median, with a 3% uncertainty in the slope of a linear correlation.

#### 4.2.2. Reducing to a Standard System: H $\alpha$

The H $\alpha$  images are calibrated to absolute flux units. No correction was made for contamination by the 2 [N II] lines ( $\lambda = 6548.1, 6583.8 \text{ \AA}$ ), which also lie within the filter bandpass. This assumption is based on the work of Kennicutt & Kent (1983) and Kennicutt (1992), who evaluate the relative [N II] contribution to the flux in H II regions. They find a median [N II]/H $\alpha$  of 0.53, with a scatter that is significantly smaller than the scatter in overall H $\alpha$  emission strengths in spiral galaxies. Hereafter we will abbreviate H $\alpha$ + [N II] as H $\alpha$ .

H $\alpha$  observations prior to 1992 were originally calibrated using the Barnes and Hayes (1984) Standard Star Manual. The fluxes based on this system appear in Young et al. (1996). In this paper, we adjust the calibration to the standard star measurements of Massey et al. (1988) for consistency between different observations and our isolated sample (11-20% lower in flux depending on standard and filter).

The measured H $\alpha$  fluxes are well correlated with those measured by Kennicutt & Kent (1983) for 23 galaxies in common, as shown in Figure 4. The solid line shows a one-to-one correlation. There is a considerable scatter, with some individual galaxies deviant by > 30%. However, most galaxies agree within 30% and the mean difference for the whole sample is close to 0. The differences for individual galaxies are most likely due to uncertainties in the continuum subtraction background sky levels, as discussed in Sections 4.3 and 4.4.

### 4.3. Sky Background Subtraction

The most important source of error in the broadband radial profiles of the outer disks of galaxies is the uncertainty in the sky background. It is therefore critical to obtain as flat a sky background as possible and carefully measure the uncertainty in the sky level. The standard deviation in the background and the uncertainty in the overall sky level were determined by measuring 4-6 blank regions of the sky, and by examining line and column plots, which were especially useful in detecting large scale gradients. Standard deviations and uncertainties in the overall sky level are listed in Table 3 in units of  $10^{-18} \text{ erg cm}^{-2} \text{ s}^{-1}$  (a zeropoint of 13.945 may be used to convert the R values to magnitudes).

Occasionally a planar gradient remained in the sky background after processing, particularly in images obtained during bright time. Where necessary, and where adequate blank sky was available, a planar surface was fit (using *imsurfit* in *iraf*) to the sky background and subtracted from the image to improve sky flatness. Where higher order gradients remained, usually due to improper flat fields or scattered light, the effect was incorporated into the sky background error.

The uncertainty in the R sky is typically 0.5-2%, except for cases in which the galaxy fills much of the CCD frame. The sky background error tends to be higher in the narrow-band H $\alpha$ , ranging from 1-6%.

### 4.4. H $\alpha$ Continuum Subtraction

Waller (1990) describes the use of broadband filters to continuum subtract narrow-line observations. We follow his procedure.

Before continuum subtraction, the R and H $\alpha$  images were background subtracted, aligned, and convolved to the same FWHM. The R image was scaled to the H $\alpha$  image based on aperture photometry of 5-15 foreground stars. This scale factor often needs adjustment, especially since the foreground field stars and the galaxy may be different in color. Adjustments were made iteratively until a satisfactory subtraction was obtained over the majority of the galaxy disk. Uncertainties in the scale factor and therefore in the estimate of the continuum level are 2-5%. Although these numbers appear small, they can result in a much higher uncertainty in the measured H $\alpha$  flux or surface brightness, since the continuum overwhelms the H $\alpha$  emission (see Section 6.3.) An additional source of uncertainty is the assumption of a constant scale factor across the galaxy, especially if there are significant color changes caused by changes in stellar populations across the disk. Assumption of a constant scale factor for the central regions and the disk is particularly problematic (see Rand 1996). Often central regions have negative residuals when the disk is well fit. Examples in this sample include NGC 4569, which has a very blue nucleus (see also Keel 1996), NGC 4694, and NGC 4527.

Ideally, foreground unsaturated stars should disappear if the images have been carefully registered and the seeing matched. However, the point spread functions are often non-Gaussian and different in the R and H $\alpha$  filters due to a number of factors, including the difference in the thicknesses of the R and H $\alpha$  filters, slight collimation errors, slight guiding errors, and differences in the focus between the two frames. Therefore, residuals often remain on the brighter stars due to imperfect continuum subtraction. (In some cases, there are systematic patterns in the stellar residuals which can be used as a diagnostic for the accuracy of the telescope collimation.) The relative fluxes of the star in the R image and the residuals in the H $\alpha$  continuum subtracted image (summing the absolute value of counts) are usually on the order of 1-2%. Residuals near the galaxy were removed using the pixel replacement routines in the IRAF task *imedit*.

Examination of the stellar residual pattern for images taken during the February 1995 run at KPNO 0.9-m telescope revealed a slight mismatch

between the pixel scales of the R and H $\alpha$  images. The IRAF tasks *geomap* and *geotran* were used to rescale the images to the same pixel scale before continuum subtraction.

The use of a broadband R filter as a substitute for an off-line narrowband filter allows significant observing time savings, making a survey of this size practical. However, there is a trade-off in accuracy (see Pogge 1992) for two reasons. Broadband and interference filters often differ in thickness and response to light, so can cause differing point-spread functions and even small plate scale differences, as noted above. In addition, the larger bandwidth of the R filter means that the derived value of the continuum is less certain and may be subject to color effects across the filter. Even small uncertainties in the continuum level are important, since they cause large uncertainties in the H $\alpha$  flux, especially in regions of weak or diffuse emission. To estimate the extent of error due to the use of a broadband filter rather than a narrowband filter, we compared 2 H $\alpha$  continuum subtracted images of the galaxy NGC 4102, kindly provided to us by Shardha Jogee. These images were taken during our February 1995 run. In one, the continuum was derived from an image taken with a narrowband H $\alpha$  offline filter ( $\lambda = 6653 \text{ \AA}$ ,  $\Delta\lambda = 68 \text{ \AA}$ ) and in the other, from a Harris R image. Stellar residuals are present in both continuum-subtracted images and differ by 2-3% in the total flux (summing the absolute value of residual counts). The total H $\alpha$  flux of the galaxy is the same to within 3%. The radial profiles in H $\alpha$  have the same shape and no systematic dependence on the continuum-subtracting filter. Aperture photometry of low H $\alpha$  surface brightness areas in the galaxy results in a 5-10% difference between the images, with the offline filter producing lower fluxes. A significant part of these differences can be attributed to uncertainties in the sky level and scale factor in each image. Based on these tests, we conclude that the R filter does a reasonable job at continuum subtracting H $\alpha$ , with error contributions smaller than the other sources of uncertainty, with the probable exception of galaxies with very weak H $\alpha$  emission.

In summary, systematic errors typically cause a 20-30% uncertainty in total H $\alpha$  fluxes and surface brightnesses.

#### 4.5. Stellar Masks

Before surface photometry can be performed on an R image, the stars must be removed or masked. DAOPHOT (Stetson 1987) was used to find stars across the image. Rather than removing the stars (which involves an iterative determination of the point spread function across the chip and does not ever fully remove stars), we chose in most cases to make a pixel mask image. In the first pass, sources found within the area of the galaxy disk were excluded from the mask, since HII regions are also detected by DAOPHOT. Stars superposed on the disk and stars missed by DAOPHOT were masked by hand using IRAF centering and the *badpixmapage* routine. Members of galaxy pairs were masked in a similar manner before surface photometry was derived. Mask images were also necessary for the H $\alpha$  image in the case of galaxy pairs or severe stellar residuals from stars which were saturated in the R image.

#### 5. The Images

R and H $\alpha$  images and surface photometry are presented for each galaxy in Figure 5. Galaxies are ordered according to NGC/IC number, with morphological information indicated on the plots. Derived photometric scalelengths are indicated in the surface photometry plots, as described in the figure caption.

#### 6. Surface Photometry

Deriving a radial profile of a galaxy consisted of several steps: determination of center, the axial ratio (ratio of minor to major axis lengths) and position angle, careful measurement of sky background error, and the surface photometry. In this section, we discuss the derivation of the radial profiles, quantities derived from the profiles, and the errors.

##### 6.1. Determining Centers, Axial Ratios, and Position Angles

The center of the galaxy was determined from the R image using centroiding via the *center* task in IRAF. Several of the galaxies (NGC 4299, NGC 4419, NGC 4424) had no obvious central peak or had a central region contaminated by bright HII

regions. In these cases, the center was determined from inner isophotes or midpoints between peaks.

Radial profiles were derived by assuming fixed values of the axial ratio and position angle, which were determined by examination of the outer isophotes. Starting values of axial ratio and position angle were determined by eye from the outer isophotes of the galaxy and/or literature inclination values (e.g., RC3, Warmels 1988). For several galaxies, including 2 of low inclination, axial ratios and/or position angles determined from HI maps (Warmels 1988) were used. For other galaxies, the axial ratios and position angles were adjusted as necessary to give a good fit to the outer isophotes.

The conversion of axial ratios to inclination angles is not well-determined (e.g. Peletier & Willner 1991). The standard conversion is  $\cos^2 i = (q^2 - q_0^2)/(1 - q_0^2)$ , where  $i$  is the inclination,  $q$  is the axial ratio, and  $q_0$  is the intrinsic axial ratio (Hubble 1926). The intrinsic axial ratio is often assumed to be 0.2 (Holmberg 1958) but it may vary with type (e.g. Bottinelli et al. 1983). The uncertainty in the conversion to inclination is most serious for galaxies of high inclination and so is not a major source of error for this study, since most sample galaxies have inclinations less than 75°. For example, the difference in inclination calculated by assuming an intrinsic axial ratio of 0 versus 0.2 is 3° at 70°. (In Section 6.3, we show the uncertainty in the radial surface brightness profiles is minor for a 5° error in the inclination.)

Adopted axial ratios and position angles are listed in columns (2) and (3) of Table 6. The inclination calculated using the standard conversion with intrinsic axial ratio of 0.2 is given in parentheses after the axial ratio. The random uncertainties in the estimation of the inclination and position angle from the outer isophotes are typically 2-3°, except in the indicated cases. Galaxies which have derived inclination and position angle significantly different from literature values are noted in the table. The H $\alpha$  profile was measured using the same center, inclination, and position angle as for the R image.

In most cases, R profiles of the galaxies were also derived by allowing the position angle, axial ratio, and center to vary with radius. This approach is useful in studying the variation in the position angle of bars, rings, and the intrinsic variation in the position angle or axial ratio,

which might indicate a recent dynamical disturbance. Position angle and/or axial ratio differences with radius are present in several galaxies in our sample. However, elliptical annuli which are allowed to vary with radius are influenced by spiral structure and are prone to errors in low surface brightness regions. In addition, the intention of this study is not to study galaxy structure in detail, but to obtain a general profile for each galaxy, which will allow us to compare the profiles and derived quantities such as concentration. For our purposes, the differences between profiles derived using fixed elliptical annuli and those using varying elliptical annuli are mostly small. A typical example is shown in Figure 6.

## 6.2. Derivation of Profiles

With the center, axial ratio, position angle, and sky background uncertainties determined (as described in Section 4.3), radial profiles were derived using a surface photometry program written within the Interactive Data Language environment, hereafter *SPHOT*. *SPHOT* allows determination of realistic errors, input of a bad pixel mask image, a correction for masked pixels to derive total flux, and simultaneous measurements of isophotal radii, concentration parameters, and integrated fluxes.

The center, axial ratio, position angle, and sky level uncertainty are read into *SPHOT*. If there is a mask image, the input image is first multiplied by the mask. Surface photometry is begun at a radius equal to one-half of the FWHM. The minimum annulus width is equal to the FWHM, and the width increases by 10% of the FWHM for each annulus, so that larger annuli are used in the outer regions where the S/N is smaller. The program calculates the surface brightness based on the unmasked pixels whose centers fall within a given annulus. The area of the annulus is calculated using the semimajor and semiminor axes of the annulus and the flux is calculated by multiplying the surface brightness by this area. This compensates for the flux from fractional and masked pixels within the annulus.

The R radial profiles were calculated out to a radius where the error in the surface brightness exceeded the signal. The errors in radial profiles are discussed in the next section.

The outermost radius of visible HII regions was determined in advance from inspection of the images, and the H $\alpha$  profile was halted just outside this radius. In some cases, especially for galaxies with faint outer disk star formation or galaxies with scattered background light or poor flat fields, this radius was beyond the point in the profile where sky uncertainty errors overwhelmed the azimuthally averaged signal. In the plots of radial profiles in Figure 5, we indicate this radius, but plot the H $\alpha$  radial profile to the outermost HII region to emphasize the extent of star formation.

All profiles were corrected to face-on assuming complete transparency in the disk, i.e., the correction  $2.5\log(a/b)$  was applied. The assumption of complete transparency is oversimplified, especially at inner radii, but since correction factors for internal extinction are poorly known, no corrections were made. (See Giovanelli et al. 1994 for more discussion.)

The inclination corrected radial profiles of individual galaxies are plotted with the images of the galaxies in Figure 5.

## 6.3. Errors in the Radial Profiles

There are several sources of errors in the calculation of the surface brightness at each radius. Processing errors contribute a relatively small percentage of the total error, and the readnoise of the chips is low. Random error is the dominant source of error in the inner regions of the surface brightness profiles and an important source of error in the integrated flux measurements. It is traced by the standard deviation in the background (e.g., Newberry 1991), which was determined using *fit-sky* or *imstat* in IRAF. In the outer parts of the profiles, large numbers of pixels are averaged to give the surface brightness, so the random error is small. In the ideal case of an accurately determined sky, the total error would be due only to the random error and would be equal to the standard deviation of the mean. However, the systematic error in determining the sky brightness overwhelms the small random error in the outer regions. It is therefore critical to obtain as flat a background as possible for deep surface photometry. The total error in the profiles was calculated by adding in quadrature the contributions from the random error and the sky uncertainty (Section 4.3).



Not included in the error calculation for individual galaxies are errors in the absolute flux calibration ( $\sim 5\%$ ) and errors in the continuum subtraction. Figure 7 shows typical errors in the  $H\alpha$  radial profile due to 2% and 5% errors in the continuum level. This Figure illustrates the sensitivity of  $H\alpha$  surface brightness to even small uncertainties in the continuum scale factor.

The radial profile is sensitive to errors in the inclination. Inclination errors are largest for highly inclined galaxies and galaxies with strong spiral arms. For most galaxies in this sample, the inclination is uncertain to less than  $3^\circ$ , as determined from the outer isophotes. The typical variation in the radial profile due to an error of  $5^\circ$  in inclination is shown for a high inclination ( $70^\circ$ ) galaxy, NGC 4419, and a low inclination ( $26^\circ$ ) galaxy, NGC 4394 in Figure 8. The uncertainty in the radial profile is small even in the case of the high inclination galaxy.

## 6.4. Derived Quantities

### 6.4.1. Isophotal Radii and Integrated Flux Measurements

A quantity useful as a galaxy size indicator is an outer isophotal radius measured in a broadband filter. R isophotal radii at 24 and, if possible, at 25 mag arcsec $^{-2}$ , were determined by interpolation of the radial profiles. 90% of the galaxies have measured radii at the 25 mag arcsec $^{-2}$  isophote. Table 6 lists the isophotal radii in units of arcsecs in columns (4) and (6) and the corresponding total R fluxes within the isophotal radius in columns (5) and (7).

Total  $H\alpha$  fluxes were measured in three different ways. Total fluxes to the radius of the outermost HII region were measured through a polygonal aperture, defined by the extent of  $H\alpha$  emission, using the *polyphot* task in IRAF. This result can be compared to the total flux measured within the outermost elliptical annulus, measured within the surface photometry program. Because the sensitivity varied between images, we also measured an integrated flux within the radius,  $r_{H\alpha 17}$ , at which the surface brightness falls to  $17 \times 10^{-18}$  erg cm $^{-2}$  s $^{-1}$ , a sensitivity level met by all the images. The three measures of the  $H\alpha$  flux are comparable. The total flux determined by surface photometry and aperture photometry are the same within

a few percent. The total flux is on the average 10% higher than the flux within  $r_{H\alpha 17}$ , but with a scatter (standard deviation) among galaxies of about 16%. This is similar to the isolated sample, which has total fluxes about 20% higher than the flux within  $r_{H\alpha 17}$ , with a 20% scatter. Two Virgo galaxies with low surface brightness, NGC 4643 and 4698, had total fluxes 3 and 9 times, respectively, higher than the flux to  $r_{H\alpha 17}$ . Finally, the  $H\alpha$  flux within  $0.3r_{24}$  and  $H\alpha$  concentration (Section 6.4.4) were measured. Table 7 presents quantities derived from the  $H\alpha$  surface photometry.

### 6.4.2. Disk Scalelengths

An isophotal radius is one type of radial normalizer. Another radial normalizer which suffers less from intrinsic surface brightness variations between galaxies is the exponential disk scalelength. The derivation of disk scalelengths is less subject to sky background problems and small frame size than derivation of isophotal radii, since the whole radial range of the light profile is used. However, the measurement of a disk scalelength is more complicated than that of a simple isophotal radius, because it is usually derived by non-linear fitting of an exponential function to the radial profile. Fitting bulge and disk models to radial profiles is a tricky task, subject to the form of the models chosen, uncertainties due to the projection of a three-dimensional distribution into the sky, seeing corrections, contamination of the profiles by star forming regions, bars, rings, dust (e.g., Giovanelli et al. 1994, 1995), and uncertainties in the background values. The greatest uncertainties are in fitting a proper bulge, especially given the discussion over exponential vs. deVaucouleurs laws (see Kormendy 1992, Courteau et al. 1996, de Jong 1996a). In order to derive a disk scalelength, we fit traditional  $r^{\frac{1}{4}}$  bulge and exponential disk models to the profiles, using the IRAF/STSDAS non-linear fitting task, *nfit1d*. We warn that extreme care must be used in applying this task, since it is very sensitive to complexities in the radial profile. The task attempts to compensate for deviations from a pure bulge + disk profile by overestimating the contribution of the bulge and/or by overemphasizing the inner disk fit compared to the outer disk fit. We report only the disk scalelength because of the 4 parameters that varied in

the bulge-disk decompositions, we find that this parameter is the most stable. (This was also noted by de Jong 1996b, who find that  $r_d$  is more stable than the central disk surface brightness.) Even so, different authors often derive different scalelengths, so we attempted to test the full range of possible disk scalelengths by fitting different radial ranges with different assumptions for the central component. Among isolated galaxies (Koopmann & Kenney 2001a) and most of the Virgo Cluster sample, the disk scalelength typically varies by 10-15% for the different fits. The central disk surface brightnesses are more dependent on the assumed form of the central component. The disk scalelength and estimate of uncertainty in arcseconds appear in columns (10) and (11) of Table 7. Disk scalelengths could not be fit to two Virgo Cluster galaxies (NGC 4383, NGC 4586). The Virgo sample has a higher proportion of complex profiles: 20% (11/53) of Virgo Cluster galaxies have derived disk scalelengths which are uncertain by > 20%, compared to 0% (0/27) of the isolated sample galaxies (Koopmann & Kenney 2001a).

If the surface brightness of disks were self-similar and all disks were exponential with measurable scalelengths,  $r_{24}$  would be perfectly correlated with  $r_d$ . We find that the correlation between these two quantities is good, with a measured ratio of  $r_{24}/r_d$  of  $3.23 \pm 0.72$  for the Virgo Cluster, compared to  $3.16 \pm 0.56$  for the sample of isolated galaxies (Koopmann & Kenney 2001a). These values are similar to that found by Giovanelli et al. (1995).

Given the systematic effects of differing surface brightnesses on isophotal radii and the difficulties of model fitting and unknown extinction values on disk scalelength, it is not obvious which radial normalizer is a better indicator of galaxy/disk size. We compared results based on both normalizers, but found that our main conclusions are independent of the normalizer. Because more galaxies could be included in the analysis and because of the more uncertain nature of disk scalelength fitting, we chose to normalize by  $r_{24}$ .

#### 6.4.3. R Concentration Parameter

Because of the subjectivity of the Hubble classification and the difficulty in deriving model-independent bulge-to-disk (B/D) ratios (section 6.4.2), we also measured a central R light

concentration index.

Central light concentration parameters are objective tracers of the radial light distribution of a galaxy (e.g., Morgan 1958; deVaucouleurs 1977; Okamura et al. 1984; Kent 1985; Abraham et al. 1994, Koopmann & Kenney 1998). Concentration parameters are correlated to B/D or bulge-to-total light ratio (deVaucouleurs 1977; Okamura et al. 1984; Kent 1985; Eder 1990, but see Naim et al. 1997) and Hubble type (Abraham et al. 1994) of spiral galaxies, although they may be less sensitive in differentiating Sa, S0, and E galaxies (Abraham et al. 1994, Smail et al. 1997, van den Bergh 1997) and they are somewhat dependent on a galaxy's surface brightness (e.g., Abraham et al. 1994). Unlike B/D, concentration parameters are independent of models assumed for galaxy components.

We define a central R light concentration parameter similar to Abraham et al. (1994):

$$C30 = \frac{F_R(0.3r_{24})}{F_R(r_{24})}$$

where  $F_R(r_{24})$  is the flux in R measured within the  $r_{24}$  isophote and  $F_R(0.3r_{24})$  is the flux within the  $0.3r_{24}$  isophote. The C30 values are computed directly from the surface photometry. We find no correlations between C30 and total R magnitude within  $r_{24}$ , inclination of the galaxy, or angular distance from M87. There is a mild dependence on surface brightness, which causes higher surface brightness galaxies to have a higher C30.

C30 can be approximately translated to B/D using the following mean [C30,B/D] pairs: [0.3,0.1], [0.4,0.3], [0.5,0.8], [0.6,1.0]. These numbers are meant to only suggest a rough scale for C30, particularly since the scatter of these numbers is at least  $\pm 0.1$ , due to uncertainties in the determination of both C30 and B/D. The correlation between central light concentration and Hubble type is discussed in Koopmann & Kenney (1998, 2001b).

#### 6.4.4. H $\alpha$ Concentration Parameter

In order to compare the concentrations of R and H $\alpha$  light, we measure a central H $\alpha$  light concentration analogous to C30:

$$CH\alpha = \frac{F_{H\alpha}(0.3r_{24})}{F_{H\alpha}}$$

where  $F_{H\alpha}$  is the total  $H\alpha$  flux and  $F_{H\alpha}(0.3r_{24})$  is the flux within the  $0.3r_{24}$  isophote. This quantity is listed in Column 7 of Table 7. A  $CH\alpha$  of 1 thus indicates that all of the  $H\alpha$  emission is located within  $0.3r_{24}$ .

To compare the relative distributions of R and  $H\alpha$  light, we normalize  $CH\alpha$  by  $C30$ :  $\frac{CH\alpha}{C30}$ . For example, this quantity is larger than 1 when the  $H\alpha$  emission is more concentrated than the R light. This quantity is listed in Column 8 of Table 7.  $H\alpha$  concentrations are compared for the two samples in Koopmann & Kenney (2001b).

## 7. Discussion

Further quantitative analyses of the spatial distributions of massive star formation in Virgo Cluster and isolated spirals are provided in Koopmann & Kenney (1998, 2001a, 2001b). Here we comment briefly on the unusual  $H\alpha$  morphology of several spirals in the Virgo Cluster sample.

It is evident from our  $H\alpha$  images (Figure 5) that there is a population of galaxies in the Virgo cluster with active star formation in the circumnuclear regions, but no other disk star formation. NGC 4064, NGC 4351, NGC 4405, NGC 4424, NGC 4522, NGC 4580, and IC3392 are examples of this class. Koopmann & Kenney (2001b) quantitatively define this class as low to intermediate light concentration galaxies which have star formation rates which are similar to isolated spirals in the circumnuclear regions, but which have no star formation in the outer 60-70% of the optical disk. We call these galaxies St (spirals with severely truncated star-forming disks), since they do not fit the standard Hubble classification criteria (see Koopmann & Kenney 1998).

St galaxies are extreme examples of what van den Bergh et al. (1990) call 'Virgo-type' galaxies, galaxies with 'with fuzzy outer regions which exhibit active star formation in their central bulges (disks?)'. The definition of this class was rather broad, including NGC 4351, NGC 4424, and IC 3392, but also galaxies such as NGC 4212, NGC 4689, and NGC 4527, which have more extended star formation in the outer disk (see Figure 5). The more general 'Virgo-type' morphology is due to the truncation of the star-forming disk in cluster galaxies, which is the primary cause of the reduction in star formation rates (Kennicutt 1983)

in Virgo Cluster galaxies (Koopmann & Kenney 2001b).

The extreme truncation of St star-forming disks, coupled with the active inner star formation is an indication that these galaxies have had interesting evolutionary histories. NGC 4424 shows evidence of a recent merger event (Kenney et al. 1996). NGC 4522 is currently being stripped by the intracluster medium (Kenney & Koopmann 1999). Others among the St class may be remnants of past intracluster medium stripping events.

The funding for this research was provided by NSF grant AST-9322779. We are grateful to Con Deliyannis for his help in obtaining observations of standard stars for the derivation of the transformation equation and Sydney Barnes, Y.-C. Kim, Raj Jain, and Charles Bailyn for obtaining several of the images in this paper during service observing runs. We thank R. Pogge for excellent advice on obtaining the best continuum subtractions and R. Kennicutt for advice and encouragement. Comments from an anonymous referee led to several improvements in the final draft. This work was substantially aided by observing support from the Kitt Peak and Cerro Tololo staff. This research has made use of the NASA/IPAC Extragalactic Database (NED) which is operated by the Jet Propulsion Laboratory, California Institute of Technology, under contract with the National Aeronautics and Space Administration. The authors and maintainers of the IRAF and STSDAS software packages and instruction manuals are also gratefully acknowledged.

## REFERENCES

- Abraham, R. G., Valdes, F., Yee, H.K.C., & van den Bergh, S. 1994, *ApJ*, 432, 75
- Barnes, J. & Hayes, D. 1984, *The IRS Standard Star Manual* (NOAO, Tucson)
- Bennett, S.M. & Moss, C. 1998, *A&A*, 132, 55
- Bicay, M. D. & Giovanelli, R. 1987, *ApJ*, 321, 645
- Binggeli, B., Sandage, A., & Tammann, G. A. 1985, *AJ*, 90, 1681 (BST)
- Binggeli, B., Tammann, G. A., & Sandage, A. 1987, *AJ* 94, 251
- Binggeli, B., Popescu, C. C., & Tammann, G. A. 1993, *A&AS*, 98, 275

- Böhringer, H., Briel, U.G., Schwarz, R.A., Voges, W., Hartner, G., Trümper, J. 1994, *Nature*, 368, 828
- Boselli, A. Tuffs, R., Gavazzi, G., Hippelein, H., Pierini, D. 1997, *A&AS*, 121, 507
- Bottinelli, L., Gouguenheim, L., Paturel, G., & de Vaucouleurs, G. 1983, *A&A*, 118, 4
- Cayatte, V., van Gorkom, J. H., Balkowski, C., & Kotanyi, C. 1990, *AJ*, 100, 604
- Courteau, S., de Jong, R. S., de Broeils, A. H. 1996, *ApJ* 457, 73
- de Jong, R. 1996a, *A&AS*, 118, 557
- de Jong, R. 1996b, *A&A*, 313, 45
- de Jong, R. & van der Kruit, P. C. 1994, *A&A Supp*, 106, 451
- deVaucouleurs, G. 1961, *ApJS*, 6, 213
- deVaucouleurs, G. 1977, in *The Evolution of Galaxies and Stellar Populations*, B. M. Tinsley & R. B. Larson (eds.) (New Haven: Yale University Observatory), p. 43
- deVaucouleurs, G., deVaucouleurs, A., Corwin, H. G., Buta, R. J., Paturel, G., Fouqué, P. 1991, *Third Reference Catalog of Bright Galaxies*, (New York: Springer-Verlag) (RC3)
- Donas, J, Buat, V., Milliard, B., & Laget, M. 1990, *A&A*, 235, 60
- Eder, J. A. 1990, Ph.D. thesis, Yale University
- Ftaclas, C., Fanelli, M.N., & Struble, M.S. 1984, *ApJ*, 282, 19
- Gavazzi, G., Boselli, A., & Kennicutt, R. 1991, *AJ*, 101, 1207
- Gavazzi, G., Boselli, A., Scodreggio, M., Pierini, D., Belsole, E. 1999, *MNRAS*, 304, 595
- Giovanelli, R., Haynes, M. P., Salzer, J. J., Wegner, G., Da Costa, L. N., & Freudling, W. 1994, *AJ*, 107, 2036
- Giovanelli, R., Haynes, M. P., Salzer, J. J., Wegner, G., Da Costa, L. N., & Freudling, W. 1995, *AJ*, 110, 1059
- Giovanelli, R. & Haynes, M. P. 1983, *AJ*, 88, 881
- González Delgado, R.M., Perez, E., Tadhunter, C., Vilchez, J., Rodríguez-Espinoza, J.M. 1997, *ApJS*, 108, 155
- Hameed, S. & Devereux, N. 1999, *AJ*, 118, 730
- Hamuy, M, Walker, A. R., Suntzeff, N. B., Gigoux, P., Heathcote, S. R., & Phillips, M. M. 1992, *PASP*, 104, 533
- Hoffman, G. L., Lewis, B. M., Helou, G., Salpeter, E. E., & Williams, H. L. 1989, 69, 65
- Hodge, P.W. & Kennicutt, R.C. 1983, *AJ*, 88, 296
- Holmberg, W. 1958, *Medd. Lunds. Astron. Obs., Ser. II*, No. 136
- Hubble, E. P. 1926, *ApJ*, 64, 321
- Jacoby, G. *et al.*, 1992, *PASP*, 104, 599
- Kelson, D. D. et al. 2000, *ApJ*, 529, 768
- Keel, W. C. 1996, *PASP*, 108, 917
- Kenney, J.D. 1987, Ph.D. thesis, University of Massachusetts, Amherst
- Kenney, J.D.P. & Young, J. 1989, *ApJ*, 344, 171
- Kenney, J. D. P., Koopmann, R. A., Rubin, V.C., & Young, J. S. 1996, *AJ*, 111, 152
- Kenney, J.D.P. & Koopmann, R.A. 1999, *AJ*, 117, 181
- Kennicutt, R. C. 1983, *AJ*, 88, 483
- Kennicutt, R. C. 1989, *ApJ*, 344, 685
- Kennicutt, R. C. 1992, *ApJ*, 388, 310
- Kennicutt, R. C. & Kent, S. M. 1983, *AJ*, 88, 1094
- Kennicutt, R. C., Bothun, G. D., & Schommer, R. A. 1984, *AJ*, 89, 179
- Kent, S. M. 1985, *ApJS*, 59, 115
- Kodaira, K., Watanabe, T., Onaka, T., & Tanaka, W. 1990, *ApJ*, 363, 422
- Koopmann, R.A. & Kenney, J.D.P. 1998, *ApJ*, 497, L75
- Koopmann, R.A. & Kenney, J.D.P. 2001a, in prep
- Koopmann, R.A. & Kenney, J.D.P. 2001b, in prep
- Kormendy, J. 1993, in *Galactic Bulges*, IAU Symposium 153, H Habing & H. Dejonghe (ed), p 209
- Kotanyi, C. G. 1980, *A&AS*, 41, 421
- Landolt, A. U. 1992a, *AJ*, 104, 340
- Landolt, A. U. 1992b, *AJ*, 104, 372
- Massey, P., Strobel, K., Barnes, J. V., & Anderson, E. 1988, *ApJ*, 328, 315
- Morgan, W. W. 1958, *PASP*, 70, 364
- Moss, C. & Whittle, M. 1993, *ApJ*, 407, L17
- Naim, A., Ratnatunga, K., & Griffiths, R. 1997, *ApJ*, 476, 510
- Newberry, M. V. 1991, *PASP*, 103, 122
- Okamura, S., Kodaira, K., & Watanabe, M. 1984, *ApJ*, 280, 7
- Peletier, R. F. & Willner, S. P. 1991, *ApJ*, 382, 382
- Pierce & Tully, R. B. 1988, *ApJ*, 330, 579
- Phillips, A.C. 1993 Ph.D. Thesis, University of Washington

- Pogge, R. W. 1992, in *Astronomical CCD Observing and Reduction Techniques*, S. B. Howell (ed), San Francisco:ASP), p. 195
- Rand, R. J. 1996, ApJ, 462, 712
- Rubin, V.C., Waterman, A.H., Kenney, J.D.P. 1999, AJ, 118,236
- Ryder, S.D., Dopita, M.A. 1993, ApJS, 88, 415
- Sandage, A. & Bedke, J. 1994, *The Carnegie Atlas of Galaxies*, (Washington: Carnegie)
- Sandage, A. & Tammann, G. A. 1987, *A Revised Shapley-Ames Catalog of Bright Galaxies*,(Washington: Carnegie) (RSA)
- Schindler, S., Binggeli, B., & Boehringer, H. 1999, A&A, 343, 420
- Schroeder, A. & Visvanathan, N. 1996, A&A Supp., 118, 441
- Smail, I. Dressler, A., Couch, W. J., Ellis, R. S., Oemler, A., Butcher, H., & Sharples, R. M. 1997, ApJS, 110, 213
- Stetson, P. B. 1987, PASP, 99, 191
- Tody, D. 1993, in *Astronomical Data Analysis Software and Systems II*, A.S.P. Conference Ser., Vol 52, eds. R.J. Hanisch, R.J.V. Brissenden, & J. Barnes (A.S.P.) 173
- Tully, R. & Shaya, E. 1984, ApJ, 281, 31
- Waller, W.H. 1990, PASP, 102, 1217
- Warmels, R. H. 1988, A&A Supp., 72, 19
- van den Bergh, S. 1997, AJ, 113, 2054
- van den Bergh, S., Pierce, M.J., & Tully, R. B. 1990, ApJ, 359, 4
- Yasuda, N., Fukugita, M., & Okamura, S. 1997, ApJS, 108, 417
- Young, J.S., Allen, L., Kenney, J.D.P., Lesser, A., & Rownd, B. 1996, AJ, 112, 1903

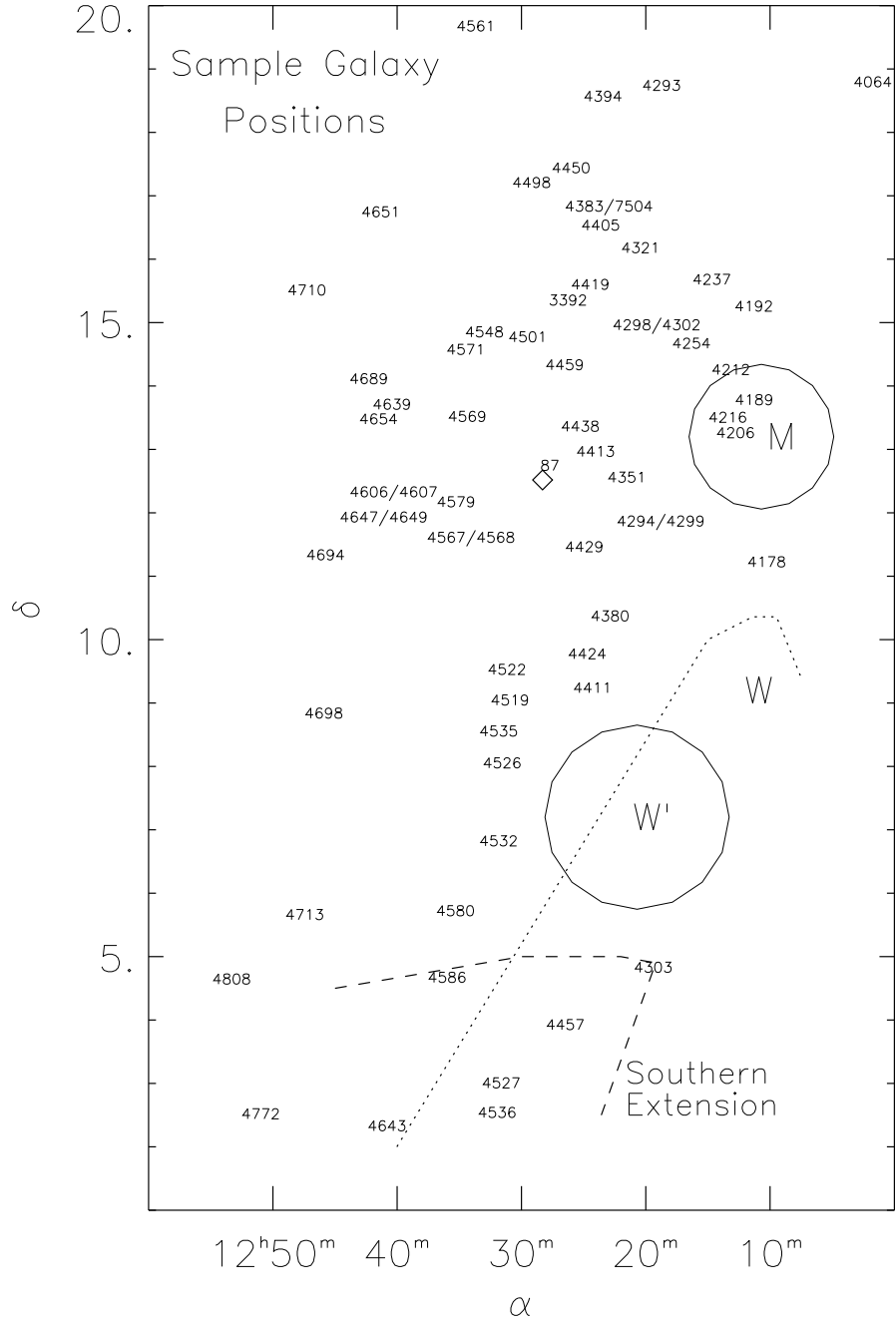


Fig. 1.— Locations of sample galaxies in the Virgo Cluster. Galaxy positions are symbolized by the NGC/IC number of the galaxy. The projected locations of the M, and W' clouds (circles), the W cloud (dotted line), and the Southern Extension (dashed lines) are indicated, based on Figure 4 from Binggeli et al. (1993). The position of M87 is indicated by the diamond.

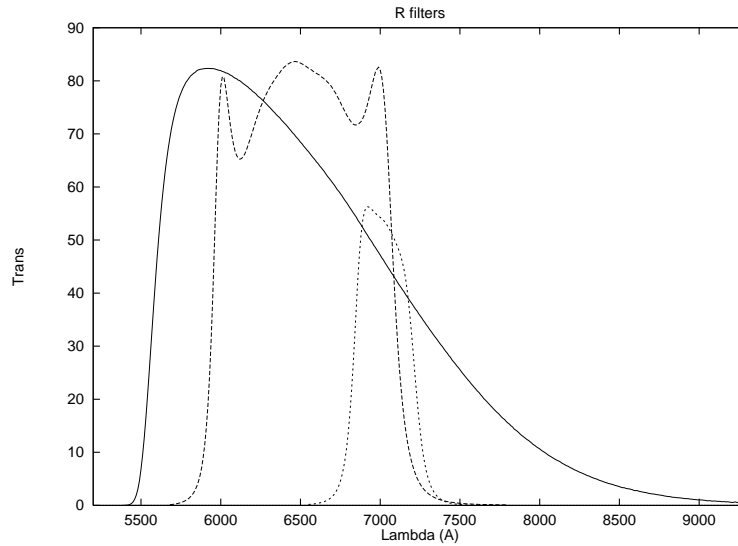


Fig. 2.— Red passband filter curves: Harris R (solid), nearly Mould R (dashed), and narrow R (dotted). Filters are respectively abbreviated as R, nmR, and sR in Table 3.

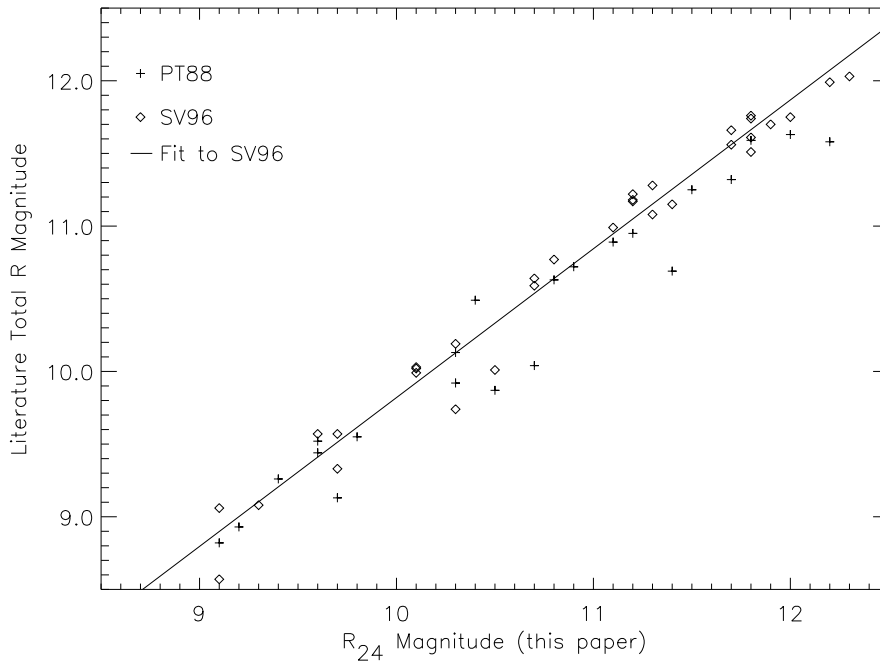


Fig. 3.— Comparison between total R magnitudes from Pierce & Tully (1988) and Schroeder & Visvanathan (1996) and the  $R_{24}$  isophotal magnitudes for galaxies in common. The solid line shows a least-squares fit to the Schroeder & Visvanathan data, with a relation  $R_{tot} = 1.02 R_{24} - 0.04$ . There is a 3% uncertainty in the slope. The Pierce & Tully data has a larger scatter, with a 5% uncertainty in the slope of a linear fit.

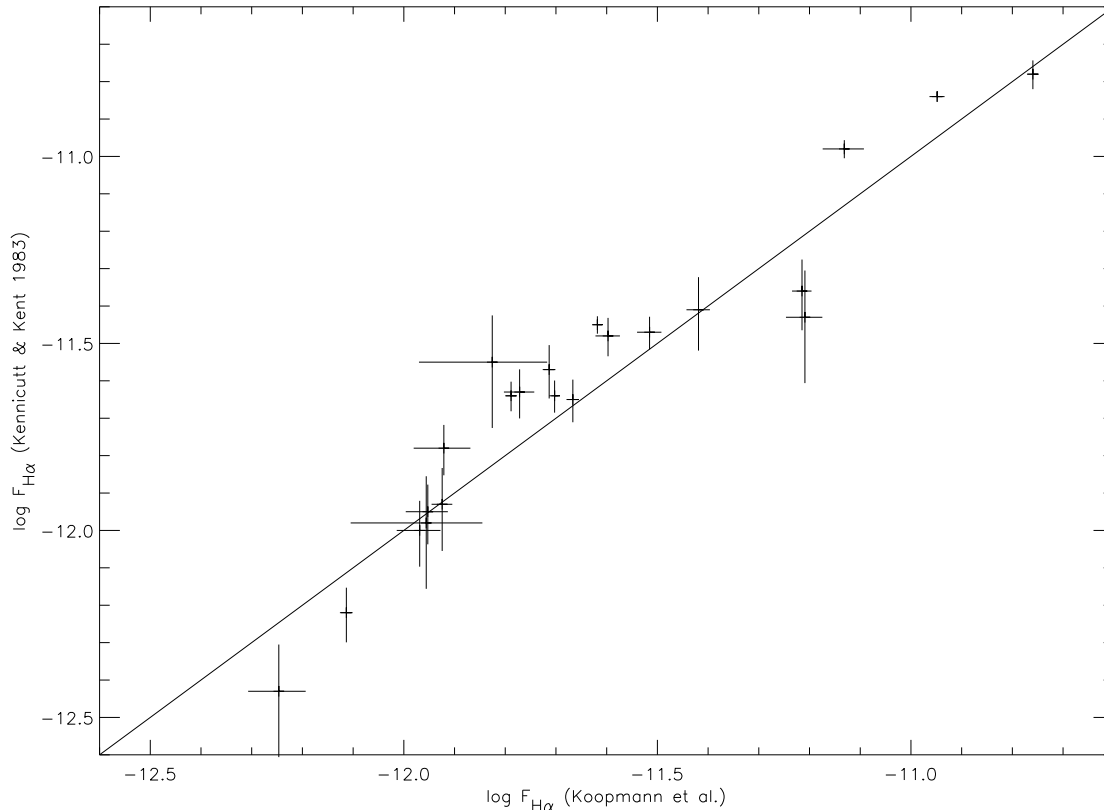


Fig. 4.— Comparison between  $H\alpha$  fluxes measured by Kennicutt & Kent (1983) and this paper for 23 galaxies in common. The solid line shows a 1:1 correspondence. The error bars for our sample are calculated by adding in quadrature the contributions from an assumed 2% continuum subtraction error and the error in the total flux due to the uncertainty in the sky background value.

Fig. 5.— The R and  $H\alpha$  images and surface photometry. Galaxies are ordered according to NGC/IC number. Images for which radial profiles were not derived appear at the end of the sequence. The images are displayed on a log scale, with north up and east to the left. The tickmarks on the images are spaced by 1.0 arcmin, and the solid line on each image represents 1 arcmin, which is equivalent to about 5 kpc for a Virgo Cluster distance of 16 Mpc. Sky around some of the larger field-of-view images was cropped; refer to Tables 3 and 4 for the actual size of the image frames. The RSA/BST morphology class is noted in the righthand corner of each image and the RSA/BST and RC3 morphological types are indicated in the surface photometry plots. In the surface photometry plots, the R (solid) and  $H\alpha$  (dotted) profiles are plotted as a function of radius in arc seconds. The  $H\alpha$  profiles were superposed using an arbitrary zeropoint of 18.945. A solid line indicating 1 kpc is provided below the morphological types. The isophotal radius at  $24 \text{ mag arcsec}^{-2}$ ,  $r_{24}$  and the disk scalelength,  $r_d$ , are indicated with arrows. An error bar for the R profile is given at  $r_{24}$ , and the R profile ends where the noise becomes greater than the signal. The  $H\alpha$  profile is cut at the radius of the outermost HII region. Diamonds on the  $H\alpha$  profile indicate annuli for which the sky uncertainty was greater than the azimuthally averaged signal. In addition, a circle is plotted on the  $H\alpha$  profile at the  $17 \times 10^{-18} \text{ erg cm}^{-2} \text{ s}^{-1} \text{ arcsec}^{-2}$  isophotal radius (which corresponds to a value of 23 R mag  $\text{arcsec}^{-2}$  in the offset scale).



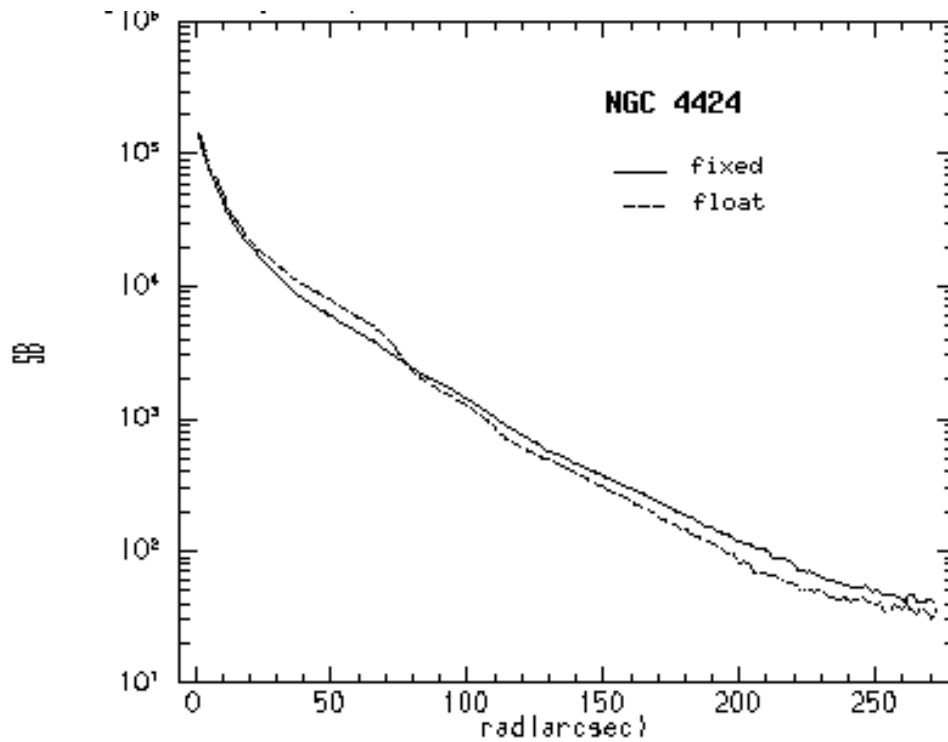


Fig. 6.— R Radial profiles of the galaxy NGC 4424. Surface brightness is in units of  $10^{-18}$  erg  $\text{cm}^{-2}$   $\text{s}^{-1}$ . The solid profile is determined using fixed center, inclination (54), and position angle (90), while the dashed profile was derived allowing center, inclination, and position angle to ‘float’ within  $130''$ . The difference in the profiles is small and does not significantly affect comparisons between large numbers of galaxies, nor the derivation of central light concentrations.

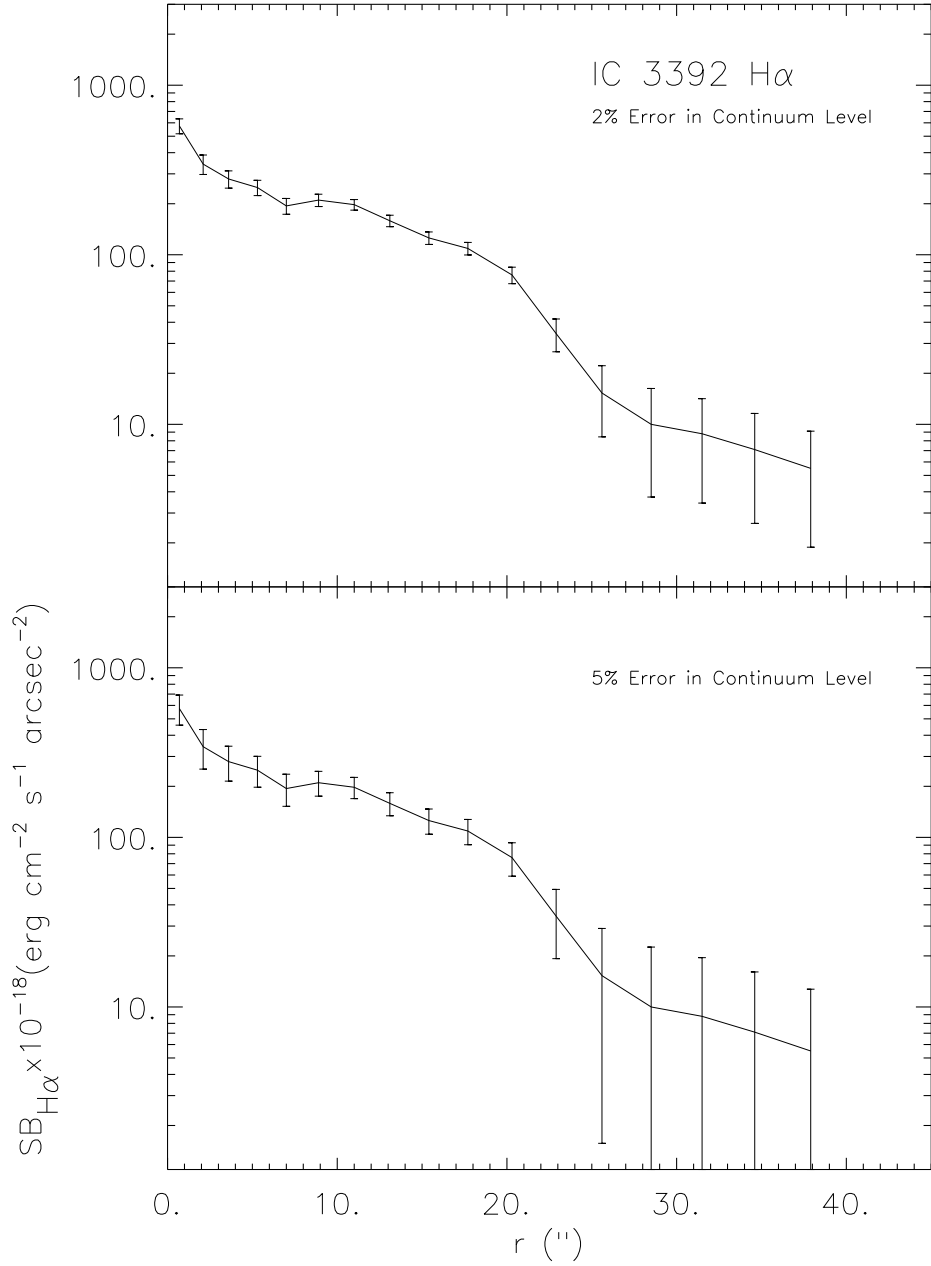


Fig. 7.— The effect of a 2% (upper) and 5% uncertainty in the continuum subtraction level on the H $\alpha$  radial profiles of IC 3392. Even small uncertainties in the continuum subtraction value can result in large uncertainties in the H $\alpha$  flux and surface brightness.

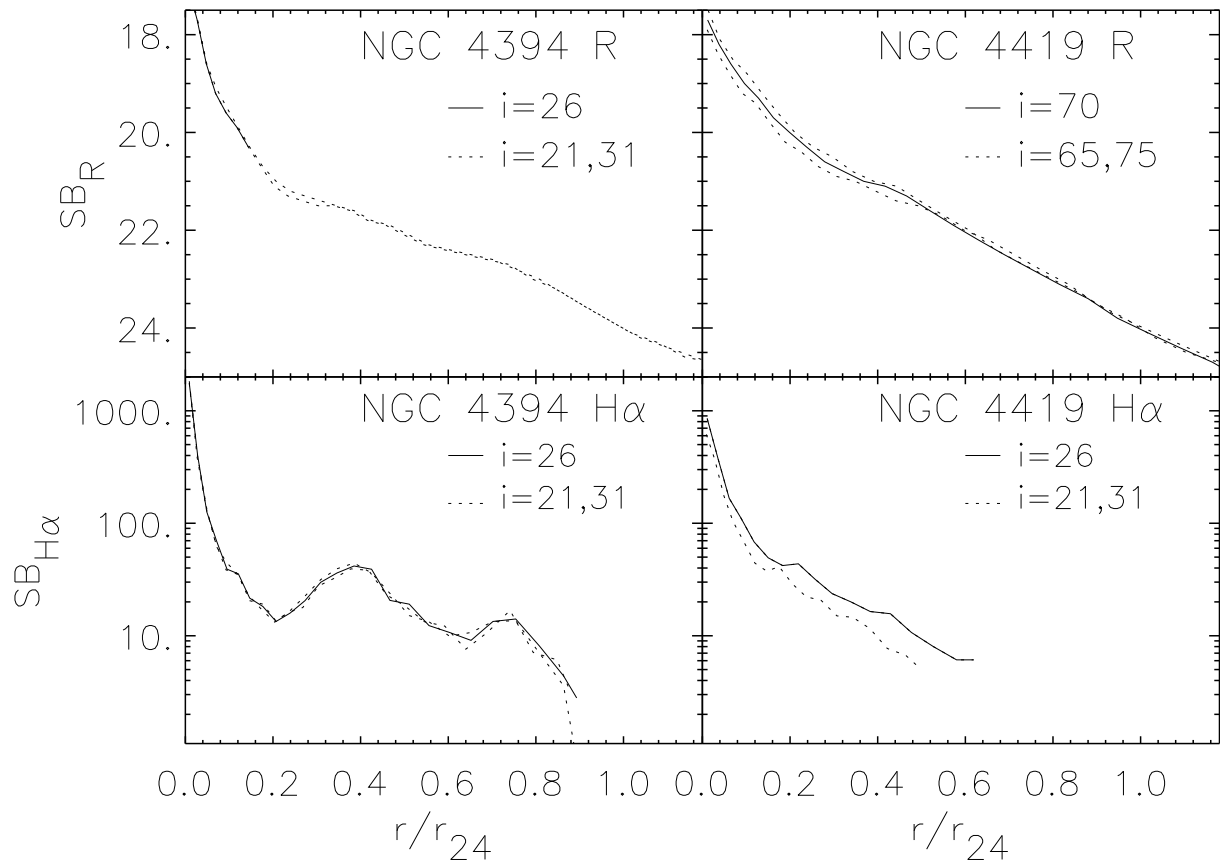


Fig. 8.— The effect of inclination error of 5 degrees on R and H $\alpha$  radial profiles of NGC 4394 (left), which has an inclination of 26°, and NGC 4419 (right), which has an inclination of 70°. Uncertainties in the radial profile due to inclination uncertainty are most severe for highly inclined galaxies. However inclination uncertainties do not strongly affect comparisons of profiles between galaxies nor derivation of central concentration.

TABLE 1  
 PROPERTIES OF OBSERVED VIRGO CLUSTER GALAXIES

(1)	(2)	(3)	(4)	(5)	(6)	(7)	(8)	(9)
Name	RA (1950) (h m s)	Dec (1950) (d m s)	RSA/BST	RC3	$B_T^O$	$v_{he}$ (km/s)	$D_{87}$ ( $^{\circ}$ )	HI Def
NGC 4064	12 01 37.8	18 43 16	SBc(s):	SB(s)a:pec	12.30	913	8.8	.99
NGC 4178	12 10 13.2	11 08 38	SBc(s)II	SB(rs)dm	11.89	378	4.7	-.13
NGC 4189	12 11 14.5	13 42 11	SBc(sr)II	SAB(rs)cd	12.53	2115	4.3	.20
NGC 4192	12 11 15.5	15 10 42	SbII:	SABab	10.92	-142	4.8	.19
NGC 4206	12 12 44.0	13 18 07	Sc(s)	Sbc:	12.77	702	3.8	.09
NGC 4212	12 13 06.6	14 10 46	Sc(s)II-III	Sc:	11.86	-81	4.0	.44
NGC 4216	12 13 21.5	13 25 40	Sb(s)	SABb:	10.97	131	3.7	.55
NGC 4237	12 14 38.9	15 36 07	Sc(r)II.2	SAB(rs)bc	12.37	867	4.4	.62
NGC 4254	12 16 17.0	14 41 39	Sc(s)I.3	Sc	10.43	2407	3.6	.02
NGC 4293	12 18 41.0	18 39 35	Sa pec	(R)SB(s)0/a pec	11.20	893	6.4	> 1
NGC 4294	12 18 45.3	11 47 10	SBc(s)II-III	SBcd	12.62	355	2.5	-.08
NGC 4298	12 19 00.6	14 53 01	Sc(s)III	Sc(rs)	12.08	1135	3.2	.54
NGC 4299	12 19 08.0	11 46 48	Scd(s)III	SABdm:	12.86	232	2.4	.05
NGC 4302	12 19 10.1	14 52 30	Sc(edge)	Sc:	12.55	1149	3.1	.43
NGC 4303	12 19 21.6	04 45 03	Sc(s)I.2	SAB(rs)bc	10.17	1566	4.8	.17
NGC 4321	12 20 22.9	16 05 58	Sc(s)I	SABbc	10.11	1571	3.9	.52
NGC 4351	12 21 29.1	12 28 54	Sc(s)II.3	SB(rs)ab:pec	13.04	2310	1.7	.58
NGC 4380	12 22 49.7	10 17 38	Sab(s)	Sb(rs):	12.36	967	2.7	1.1
NGC 4383	12 22 53.8	16 44 49	Amorph	Sa pec	12.68	1710	4.3	-.39
NGC 4394	12 23 24.3	18 29 26	SBb(sr)I-II	RSBb?	11.76	922	5.9	1.1
NGC 4405	12 23 35.5	16 27 28	Sc/S0	SA(rs)0/a	12.99	1747	4.0	1.1
NGC 4411B	12 24 14.8	09 09 41	Sc(s)II	SABcd	12.92	1270	3.6	.31
NGC 4413	12 24 00.2	12 53 16	SBbc(rs)II-III	SBab:	12.97	102	1.1	.90
NGC 4419	12 24 24.7	15 19 24	Sa	SBa(sp)	12.13	-261	2.8	1.1
NGC 4424	12 24 39.0	09 41 51	Sa pec	SAB0p	12.32	439	3.1	1.1
NGC 4429	12 24 54.1	11 23 05	S0 <sub>3</sub> (6)/Sa pec	SA(r)0 <sup>+</sup>	10.9	1130	1.5	> 1
NGC 4438	12 25 13.6	13 17 07	Sb(tides)	SA(S)0/a pec	10.91	71	1.0	1.6
NGC 4450	12 25 58.0	17 21 42	Sab pec	SAab	10.93	1954	4.7	1.3
IC 3392	12 26 11.7	15 16 34	Sc/Sa	SAb:	13.30	1687	2.7	1.4
NGC 4457	12 26 26.0	03 50 51	RSb(rs)II	(R)SAB(s)0/a	11.76	882	8.8	.83
NGC 4459	12 26 28.3	14 15 20	S0 <sub>3</sub> (2)	SA0(late)	11.37	1210	1.6	> 1
NGC 4498	12 29 08.6	17 07 41	SBc(s)II	SABd	12.62	1507	4.5	.37
NGC 4501	12 29 27.5	14 41 43	Sbc(s)II	SAb	10.27	2281	2.0	.47
NGC 4519	12 30 58.0	08 55 49	SBc(rs)II.2	SBd	12.34	1220	3.8	-.28
NGC 4522	12 31 07.6	09 27 03	Sc/Sb:	SBcd:(sp)	12.73	2328	3.3	.60
NGC 4526	12 31 30.4	07 58 33	S0 <sub>3</sub> (6)	SAB0:	10.61	448	4.8	> 1
NGC 4527	12 31 35.5	02 55 45	SB(s)II	SABbc	11.32	1736	9.8	-.35
NGC 4532	12 31 46.7	06 44 39	SmIII	Im	12.30	2012	6.0	-.30
NGC 4535	12 31 48.0	08 28 26	SBc(s)I.3	SABc	10.51	1961	4.3	.17
NGC 4536	12 31 53.5	02 27 50	Sc(s)I	SABbc	11.01	1804	10.2	.03

TABLE 1—*Continued*

(1) Name	(2) RA (1950) (h m s)	(3) Dec (1950) (d m s)	(4) RSA/BST	(5) RC3	(6) $B_T^0$	(7) $v_{he}$ (km/s)	(8) $D_{87}$ ( $^\circ$ )	(9) HI Def
NGC 4548	12 32 55.2	14 46 20	SBb(rs)I-II	SBb	10.98	486	2.4	.86
NGC 4561	12 33 38.0	19 35 53	SBcIV	SBdm	12.96:	1407	7.0	-.33
NGC 4567	12 34 01.0	11 31 59	Sc(s)II-III	SAbc	12.08	2274	1.8	.64
NGC 4568	12 34 02.5	11 30 50	Sc(s)III	SAbc	11.70	2255	1.8	.64
NGC 4569	12 34 18.5	13 26 16	Sab(s)I-II	SABab	10.25	-235	1.7	.99
NGC 4571	12 34 25.3	14 29 33	Sc(s)II-III	SAd	11.81	342	2.4	.44
NGC 4579	12 35 12.0	12 05 34	Sab(s)II	SABb	10.56	1519	1.8	1.0
NGC 4580	12 35 15.9	05 38 36	Sc/Sa	SABa?	12.49	1034	2.5	1.3
NGC 4586	12 35 55.1	04 35 37	Sa	SAa:	12.54	794	8.3	1.2
NGC 4606	12 38 26.2	12 11 09	Sa pec	SBa:	12.69	1664	2.5	>1
NGC 4607	12 38 41.0	12 09 36	...	SBb?sp	12.79	2257	2.6	.74
NGC 4639	12 40 21.5	13 31 52	SBb(r)II	SABbc	12.19	1010	3.1	.16
NGC 4643	12 40 46.9	02 15 06	...	SB(rs)0/a	11.54	1399	10.9	> 1
NGC 4647	12 41 01.1	11 51 20	Sc(rs)III	SABc	12.03	1422	3.2	.51
NGC 4649	12 41 08.4	11 49 34	S0 <sub>1</sub> (2)	E2	9.81	1413	3.2	> 1
NGC 4651	12 41 12.4	16 40 01	Sc(r)I-II	SAc	11.36	805	5.1	-.16
NGC 4654	12 41 25.9	13 23 59	SBc(rs)II	SABcd	11.14	1035	3.3	0
NGC 4689	12 45 15.0	14 02 10	Sc(s)II.3	SAbc	11.55	1616	3.7	1.1
NGC 4694	12 45 44.0	11 15 28	Amorph	SB0 pec	12.19	1175	4.5	1.2
NGC 4698	12 45 51.3	08 45 35	Sa	SAab	11.53	1002	5.8	.25
NGC 4710	12 47 09.0	15 26 15	S0 <sub>3</sub> (9)	S0 <sup>+</sup> ?(sp)	11.85	1129	5.4	> 1
NGC 4713	12 47 25.4	05 34 59	SBc(s)II-III	SABd	12.21	653	8.5	-.13
NGC 4772	12 50 55.9	02 26 27	...	SA(s)a	11.89	1040	11.7	.51
NGC 4808	12 53 17.0	04 34 28	Sc(s)III	SAbc:	12.56:	766	10.2	-.68

NOTE.— (1) Name of galaxy, (2) and (3) Galaxy Coordinates (Epoch 1950.0), (4) Hubble types from BST or Sandage & Tammann (1987) or Sandage & Bedke (1994), (5) Hubble type from deVaucouleurs et al. (1991), (6) the total, face-on blue magnitude ( $B_T^0$ ) from deVaucouleurs et al. (1991), (7) the heliocentric radial velocity, (8) the projected angular distance in degrees of the galaxy from M87, and (9) the HI deficiency parameter, which was calculated following the prescription of Giovanelli & Haynes (1983).

TABLE 2  
 COMPLETENESS BY HUBBLE TYPE AND B MAGNITUDE IN BST REGION

Type	$B_T^0 \leq 12$	$12 \leq B_T^0 \leq 13$
S0-S0/a	29% (4/14)	0% (0/16)
Sa-Sab	83% (5/6)	33% (4/12)
Sb-Sbc	100% (5/5)	100% (2/2)
Sc-Scd	100% (11/11)	55% (11/20)
Sd-Sm	- (0/0)	100% (1/1)
Amorph	- (0/0)	100%(2/2)

NOTE.—Completeness by Hubble type and total B magnitude for sample galaxies within the BST survey region.

TABLE 3  
VIRGO CLUSTER OBSERVING LOG

(1) Name	(2) Date	(3) Tel/Chip	(4) R Filt H $\alpha$ Filt	(5) R Exp H $\alpha$ Exp	(6) R X H $\alpha$ X	(7) FWHM (')	(8) R $\sigma_b$ H $\alpha$ $\sigma_b$	(9) R $\delta_s$ H $\alpha$ $\delta_s$
NGC 4064	04/01/89	KP9/TEK1	nmR	420	1.38	1.6	614	110
			H $\alpha$ 1	4000	1.27		44	7
NGC 4178	03/23/87	KP9/TI2	sR,R	3300	1.60	3.0	197	124
			H $\alpha$ 1	3900	1.28		23	7
NGC 4189	03/26/88	KP9/TI2	nmR	450	1.49	1.8	362	180
			H $\alpha$ 2	4500	1.30		39	14
NGC 4192	03/31/89	KP9/TEK1	nmR	420	1.64	2.5	420	504
			H $\alpha$ 1	4000	1.44		45	5
NGC 4206	04/02/89	KP9/TEK1	nmR	420	1.88	...	702	...
			H $\alpha$ 1	4000	1.59		67	...
NGC 4212	02/15/97	WIYN/S2KB	R	180	1.32	2.6	175	75
	03/22/87	KP9/TI2	sR	3000	1.05	3.1	...	...
			H $\alpha$ 1	3000	1.09		16	5
NGC 4216	04/01/89	KP9/TEK1	nmR	250	1.14	...	...	...
			H $\alpha$ 1	2500	1.10	...	...	...
NGC 4237	03/30/89	KP9/TEK1	nmR	420	1.77	2.2	465	153
			H $\alpha$ 1	4000	1.52		47	8
NGC 4254	03/24/87	KP9/TI2	nmR	250	1.13	2.1	300	141
			H $\alpha$ 2	3000	1.21		20	8
NGC 4293	03/25/88	KP9/TI2	nmR	300	1.17	2.2	300	219
			H $\alpha$ 1	3600	1.32		34	41
NGC 4294	03/31/89	KP9/TEK1	nmR	420	1.26	1.9	169	132
			H $\alpha$ 1	4000	1.17		24	8
NGC 4298/ NGC 4302	03/31/89	KP9/TEK1	nmR	420	1.07	1.8	460	110
			H $\alpha$ 1	4000	1.06		24	8
NGC 4299	03/30/89	KP9/TEK1	nmR	420	1.30	1.8	153	219
			H $\alpha$ 1	4000	1.17		24	7
NGC 4303	03/29/88	KP9/TI2	nmR	200	1.25	2.6	880	530
			H $\alpha$ 2	2000	1.16		31	14
NGC 4321	02/09/99	CT9/TEK2K	R	2x300	1.45	1.5	380	127
	03/24/87	KP9/TI2	nmR	230	2.01	2.0	600	...
			H $\alpha$ 2	2000	1.59		47	6
NGC 4351	03/31/89	KP9/TEK1	nmR	420	1.80	2.4	395	110
			H $\alpha$ 2	4000	1.13		37	8
NGC 4380	04/01/89	KP9/TEK1	nmR	420	1.10	1.6	307	110
			H $\alpha$ 1	4000	1.90		42	8
NGC 4383/ UGC 7504	02/04/95	KP9/t2ka	R	3x240	1.20	1.4	205	43
			H $\alpha$ 4	3x1200	1.16		22	9
NGC 4394	03/30/89	KP9/TEK1	nmR	420	1.05	1.8	153	153
			H $\alpha$ 1	4000	1.05		25	8

TABLE 3—*Continued*

(1)	(2)	(3)	(4)	(5)	(6)	(7)	(8)	(9)
Name	Date	Tel/Chip	R Filt H $\alpha$ Filt	R Exp H $\alpha$ Exp	R X H $\alpha$ X	FWHM (')	R $\sigma_b$ H $\alpha$ $\sigma_b$	R $\delta_s$ H $\alpha$ $\delta_s$
NGC 4405	03/02/95	KP9/t2kA	R	2x450	1.04	1.3	170	43
			H $\alpha$ 4	3x1800	1.05		22	9
NGC 4411B	04/02/89	KP9/TEK1	nmR	420	1.20	2.2	220	220
			H $\alpha$ 2	4000	1.28		29	8
NGC 4413	03/26/88	KP9/TI2	nmR	900	1.07	1.5	120	88
			H $\alpha$ 1	4500	1.08		22	7
NGC 4419	02/15/97	WIYN/S2KB	R	180	1.30	1.9	156	156
	03/26/87	KP9/TI2	sR	600	1.83	1.7	...	...
			H $\alpha$ 1	1200	1.61		18	4
NGC 4424	02/02/95	KP9/t2ka	R	6x600	1.15	1.4	93	105
	04/02/89	KP9/TEK1	nmR	420	1.4	2.0	658	313
			H $\alpha$ 1	400	1.28		51	13
NGC 4429	02/05/95	KP9/t2ka	R	4x135	1.09	1.1	311	108
			H $\alpha$ 3	3x1200	1.07		26	11
NGC 4438	04/02/89	KP9/TEK1	nmR	420	1.06	2.2	592	219
			H $\alpha$ 2	3000	1.50		64	5
NGC 4450	04/01/89	KP9/TEK1	nmR	300	1.06	1.7	395	164
			H $\alpha$ 2	3000	1.11		42	8
IC 3392	02/03/95	KP9/t2ka	R	3x300	1.18	1.2	150	43
			H $\alpha$ 4	3x1800	1.11		20	9
NGC 4457	03/03/93	CT9/TEK1K-1	R	300	1.28	1.9	714	320
			H $\alpha$	3x2400	1.22		38	13
NGC 4459	03/30/89	KP9/TEK1	nmR	250	1.06	2.1	395	219
			H $\alpha$ 2	3000	1.11		33	20
NGC 4498	04/01/89	KP9/TEK1	nmR	420	1.25	1.6	130	88
			H $\alpha$ 2	4000	1.43		25	8
NGC 4501	03/29/88	KP9/TI2	nmR	250	1.89	2.6	1266	527
			H $\alpha$ 2	2000	1.70		136	27
NGC 4519	03/26/88	KP9/TI2	nmR	600	1.13	1.6	123	105
			H $\alpha$ 2	3600	1.15		25	14
NGC 4522	04/02/89	KP9/TEK1	nmR	420	1.16	2.0	153	110
			H $\alpha$ 2	4000	1.12		24	5
NGC 4526	03/25/88	KP9/TI2	nmR	120	1.16	2.0	350	175
			H $\alpha$ 1	2000	1.70		35	40
NGC 4527	03/25/87	KP9/TI2	nmR	450	1.23	1.9	230	176
			H $\alpha$ 2	2500	1.46		25	8
NGC 4532	03/26/88	KP9/TI2	nmR	900	1.23	1.7	97	176
			H $\alpha$ 2	3600	1.15		25	10
NGC 4535	03/29/88	KP9/TI2	nmR	300	1.67	2.2	1406	176
			H $\alpha$ 2	2500	1.46		115	20



TABLE 3—*Continued*

(1) Name	(2) Date	(3) Tel/Chip	(4) R Filt H $\alpha$ Filt	(5) R Exp H $\alpha$ Exp	(6) R X H $\alpha$ X	(7) FWHM (')	(8) R $\sigma_b$ H $\alpha$ $\sigma_b$	(9) R $\delta s$ H $\alpha$ $\delta s$
NGC 4536	03/30/89	KP9/TEK1	nmR H $\alpha$ 2	400 4000	1.29 1.45	1.8	208 35	219 13
NGC 4548	03/29/88	KP9/TI2	nmR H $\alpha$ 1	300 2700	1.50 1.06	3.6	770 81	176 16
NGC 4561	03/26/87	KP9/TI2	nmR H $\alpha$ 2	500 6600	1.03 1.31	2.1	105 16	53 7
NGC 4567	03/31/89	KP9/TEK1	nmR	420	1.23	1.7	147	219
NGC 4568			H $\alpha$ 2	4000	1.40		24	8
NGC 4569	03/25/88	KP9/TI2	nmR H $\alpha$ 1	150 3000	1.15 1.10	2.0	240 41	316 68
NGC 4571	02/15/97 03/23/87	WIYN/s2kb KP9/TI2	R sR H $\alpha$ 1	180 2500 4500	1.09 1.09 1.05	3.0 2.2	156 ... 16	150 ... 7
NGC 4579	03/29/88	KP9/TI2	nmR H $\alpha$ 2	250 1500	1.07 1.06	2.6	880 110	353 16
NGC 4580	02/02/95	KP9/t2ka	R H $\alpha$ 3	3x450 3x1800	1.23 1.12	1.4	162 20	43 11
NGC 4586	04/09/92	CT9/TEK1K	R H $\alpha$ 5	6x300 4x1200	1.31 1.28	6.3	300 ...	160 ...
NGC 4606/ NGC 4607	02/06/95	CT9/t2ka	R H $\alpha$ 4	3x240 4x900	1.23 1.18	1.4	205 26	65 11
NGC 4639	03/31/89	KP9/TEK1	nmR H $\alpha$ 1	420 4000	1.66 2.26	2.1	79 14	329 16
NGC 4643	02/04/96	CT9/TEK2K	R H $\alpha$ 6	2x300 4x1350	1.20 1.22	1.5	860 20	450 19
NGC 4647/ NGC 4649	03/30/89	KP9/TEK1	nmR H $\alpha$ 2	350 4000	1.51 1.87	1.9	175 19	329 8
NGC 4651	02/15/97 03/23/87	WIYN/s2kb KP9/TI2	R sR H $\alpha$ 1	180 900 2500	1.19 2.01 1.68	2.2 2.0	156 ... 16	94 ... 8
NGC 4654	03/26/87	KP9/TI2	nmR H $\alpha$ 2	500 4000	2.14 1.74	2.1	141 24	176 11
NGC 4689	02/15/97 03/25/87	WIYN/s2kb KP/TI2	R sR H $\alpha$ 2	180 2500 4000	1.23 1.06 1.29	2.0 2.2	230 ... 18	125 ... 7
NGC 4694	02/04/95	KP9/t2ka	R H $\alpha$ 3	2x450 3x1200	1.12 1.09	1.5	173 17	43 11
NGC 4698	02/05/95	KP9/t2ka	R H $\alpha$ 3	3x180 3x900	1.34 1.26	1.2	280 15	65 9
NGC 4710	03/26/87	KP9/TI2	nmR H $\alpha$ 2	300 1850	1.36 1.11	1.7	510 40	175 41

TABLE 3—*Continued*

(1) Name	(2) Date	(3) Tel/Chip	(4) R Filt H $\alpha$ Filt	(5) R Exp H $\alpha$ Exp	(6) R X H $\alpha$ X	(7) FWHM (')	(8) R $\sigma_b$ H $\alpha$ $\sigma_b$	(9) R $\delta s$ H $\alpha$ $\delta s$
NGC 4713	03/26/87	KP9/TI2	nmR	800	1.18	2.0	79	108
			H $\alpha$ 1	3800	1.12		19	11
NGC 4772	02/25/93	CT9/TEK2K	R	1x900	1.33	2.4	446	128
			H $\alpha$ 5	2x2400	1.19		51	16
NGC 4808	02/15/97	WIYN/s2kb	R	180	1.20	2.5	160	94
	03/23/87	KP9/TI2	sR	1500	1.20	2.1	...	...
			H $\alpha$ 1	4000	1.27		18	7

NOTE.— (1) name of the galaxy, (2) the date of the observation, (3) the telescope and chip (where chip characteristics are listed in Table 4, and KP9 means Kitt Peak 0.9 m and CT9 means CTIO 0.9m), (4) filter code (listed in Table 5), (5) exposure time in seconds, (6) airmass of the observation, (7) the full width half maximum (FWHM) in arcseconds of the processed images (the R and H $\alpha$  images were convolved to the same seeing in the reduction process), (8) the sky background sigma, (9) and the estimated uncertainty in the sky background level. The units of columns (8) and (9) are  $10^{-18}$  erg cm $^{-2}$  s $^{-1}$  arcsec $^{-2}$ . R flux values may be converted to magnitudes using a zeropoint of 13.945.

TABLE 4  
CHIP CODES AND CHARACTERISTICS

Detector	Scale ( $'' \text{ pix}^{-1}$ )	Size (pix)	FOV ( $'$ )
TI2	0.86	396	5.7
TEK1	0.77	512	6.6
t2ka	0.68	2048	23.2
TEK2K	0.40	2048	13.7
TEK1K	0.40	1024	6.8
s2kb	0.20	2048	6.8

TABLE 5  
FILTER CHARACTERISTICS

Filter	$\lambda_{cent}$ ( $\text{\AA}$ )	$\delta\lambda$ ( $\text{\AA}$ )
H $\alpha$ 1	6563	80
H $\alpha$ 2	6608	76
H $\alpha$ 3	6573	68
H $\alpha$ 4	6618	74
H $\alpha$ 5	6563	78
H $\alpha$ 6	6606	75
R	6425	1540
nmR	6470	1110
sR	7024	380

TABLE 6  
PARAMETERS AND DERIVED QUANTITIES FOR THE R SURFACE PHOTOMETRY

(1)	(2)	(3)	(4)	(5)	(6)	(7)	(8)	(9)	(10)
Name	Inc	PA	r <sub>24</sub>	R <sub>24</sub>	r <sub>25</sub>	R <sub>25</sub>	C30	r <sub>d</sub>	Δ r <sub>d</sub>
	(°)	(°)	( $''$ )	(mag)	( $''$ )	(mag)		( $''$ )	( $''$ )
NGC 4064	0.391 (70)	150	104	11.2	138	11.1	0.43	44	2
NGC 4178	0.342 (74)	33	119	11.4	146	11.2	0.25	45	4
NGC 4189	0.695 (47) <sup>a</sup>	70 <sup>b</sup>	72	11.5	86	11.4	0.29	20	5
NGC 4192	0.276 (79) <sup>c</sup>	155	218	9.7	260	9.6	0.34	72	4
NGC 4212	0.643 (51) <sup>d</sup>	75	89	10.7	104	10.6	0.39	22	4
NGC 4237	0.682 (48)	108	69	11.2	92	11.2	0.47	16	4
NGC 4254	0.839 (34)	57:	150	9.4	178	9.4	0.46	33	3
NGC 4293	0.438 (67)	66 <sup>a</sup>	162	10.1	216	10.0	0.40	60	5
NGC 4294	0.391 (70)	155	74	11.8	92	11.7	0.33	22	2
NGC 4298	0.530: (60)	135	109	10.8	153	10.8	0.36	32	3
NGC 4299	0.927: (22) <sup>e</sup>	96 <sup>f</sup>	52	12.2	0	0.0	0.33	15	4
NGC 4303	0.906 (26)	42	177	9.2	0	0.0	0.51	42	3
NGC 4321	0.875 (30) <sup>f</sup>	153 <sup>f</sup>	239	9.1	319	9.0	0.40	75	4
NGC 4351	0.695 (47) <sup>a</sup>	80	62	12.3	92	12.1	0.37	25	5
NGC 4380	0.530 (60)	158	104	11.1	129	11.0	0.33	35	5
NGC 4383	0.643 (51) <sup>a</sup>	15 <sup>a</sup>	61	11.7	87	11.6	0.63	...	...
NGC 4394	0.906 <sup>e</sup> (26)	108 <sup>e</sup>	112	10.5	145	10.5	0.47	33	2
NGC 4405	0.695 (47) <sup>a</sup>	15	54	11.8	69	11.8	0.47	18	5
NGC 4411B	1.00 (0) <sup>e</sup>	0: <sup>e</sup>	80	12.1	99	12.0	0.32	29	2
NGC 4413	0.656 (50)	60	65	11.9	86	11.9	0.37	20	2
NGC 4419	0.391 (70)	133	84	10.7	103	10.6	0.52	20	2
NGC 4424	0.616 (54) <sup>a</sup>	90	93	11.2	125	11.1	0.42	33	4
NGC 4429	0.500 (62)	90: <sup>a</sup>	171	9.7	220	9.7	0.54	57	4
NGC 4450	0.707 (46)	175	166	9.6	205	9.5	0.49	41	4
IC 3392	0.454 (65)	37	66	11.8	91	11.8	0.37	22	5
NGC 4457	1.00: (0) <sup>e</sup>	0: <sup>e</sup>	128	10.1	0	0.0	0.66	40	3
NGC 4459	0.819 (36)	110	138	10.0	177	10.0	0.71	40	3
NGC 4498	0.485 (63)	136	75	12.0	95	11.9	0.31	25	2
NGC 4501	0.50 (62)	140	185	9.1	0	0.0	0.45	46	3
NGC 4519	0.743 (43)	146	73	11.8	85	11.8	0.35	21	4
NGC 4522	0.276 (79)	36	78	12.2	107	12.0	0.28	30	3
NGC 4527	0.309 (76)	67	157	10.1	214	10.0	0.42	50	5
NGC 4532	0.391 (70) <sup>g</sup>	160	66	11.7	89	11.7	0.39	18	3
NGC 4535	0.731 (44)	0	174	9.8	0	0.0	0.29	60	6
NGC 4536	0.391 (70)	125	190	10.1	231	10.0	0.36	70	7
NGC 4548	0.809 (37)	136 <sup>f</sup>	162	9.6	191	9.6	0.43	50	5
NGC 4561	0.829 (35)	35	46	12.5	63	12.4	0.39	18	4
NGC 4567	0.695 (47)	85	113	10.9	141	10.9	0.50	31	3
NGC 4568	0.438 (67)	23	128	10.5	165	10.4	0.44	36	3
NGC 4569	0.469 (64)	23	209	9.3	266	9.3	0.43	66	4

TABLE 6—*Continued*

(1)	(2)	(3)	(4)	(5)	(6)	(7)	(8)	(9)	(10)
Name	Inc	PA	$r_{24}$	$R_{24}$	$r_{25}$	$R_{25}$	C30	$r_d$	$\Delta r_d$
	( $^\circ$ )	( $^\circ$ )	( $''$ )	(mag)	( $''$ )	(mag)		( $''$ )	( $''$ )
NGC 4571	0.829 (35) <sup>a</sup>	40 <sup>a</sup>	120	10.8	152	10.7	0.34	40	4
NGC 4579	0.799 (38)	95	166	9.2	0	0.0	0.52	42	3
NGC 4580	0.719 (45)	158 <sup>a</sup>	72	11.3	87	11.3	0.41	19	5
NGC 4586	0.342 (74)	114	129	11.4	165	11.3	0.56	...	...
NGC 4606	0.438 (67)	40 <sup>a</sup>	76	11.8	103	11.7	0.42	25	5
NGC 4639	0.669 (49)	123	79	11.2	100	11.1	0.50	20	2
NGC 4643	0.777 (40)	30 <sup>a</sup>	141	10.0	0	0.0	0.60	45	4
NGC 4647	0.809 (37)	100 <sup>a</sup>	86	10.9	0	0.0	0.40	25	3
NGC 4651	0.642 (51)	71 <sup>af</sup>	115	10.3	157	10.2	0.55	26	5
NGC 4654	0.629 (52)	125	119	10.5	158	10.5	0.35	36	3
NGC 4689	0.819 (36)	166	143	10.4	195	10.3	0.38	50	5
NGC 4694	0.755 (42)	140	85	11.3	120	11.2	0.62	40	3
NGC 4698	0.500 (62) <sup>a</sup>	168	127	10.3	187	10.2	0.51	70	5
NGC 4713	0.656 (50)	95	68	11.6	78	11.6	0.35	17	4
NGC 4772	0.500 (62)	145	117	10.9	144	10.9	0.51	42	4
NGC 4808	0.391 (70)	127	69	11.5	83	11.4	0.38	19	4

NOTE.— (1) Name of galaxy, (2) axial ratio and, in parentheses, inclination calculated using the Hubble (1926) conversion (see Section 6.1, (3) position angle, (4)  $r_{24}$ , the radius in units of arcsecs at the 24 R mag/arcsec<sup>2</sup> isophote, (5) the magnitude within  $r_{24}$ , (6)  $r_{25}$ , the radius in units of arcsecs at the 25 R mag/arcsec<sup>2</sup> isophote, (7) the magnitude within  $r_{25}$ , (8) the central R light concentration parameter, (9) the disk scalelength, and (10) the uncertainty in the disk scalelength.

<sup>a</sup>Pierce & Tully (1988) inclination of 55 $^\circ$  not supported by outer isophotes

<sup>b</sup>Value different by more than 5 $^\circ$  from RC3.

<sup>c</sup>Pierce & Tully (1988) inclination of 86 $^\circ$  not supported by outer isophotes; Warmels (1988) HI analysis indicates an inclination of 70 $^\circ$ .

<sup>d</sup>Pierce & Tully (1988) inclination of 44 $^\circ$  not supported by outer isophotes

<sup>e</sup>Galaxy is close to face-on, so the inclination and position angle are less certain.

<sup>f</sup>Value taken from Warmels (1988).

<sup>g</sup>Pierce & Tully (1988) inclination of 61 $^\circ$  not supported by outer isophotes

TABLE 7  
PARAMETERS AND DERIVED QUANTITIES FROM THE H $\alpha$  SURFACE PHOTOMETRY

(1) Name	(2) log F $_{H\alpha}$	(3) r $_{HII}$ (")	(4) r $_{H\alpha 95}$ (")	(5) r $_{H\alpha 17}$ (")	(6) log F $_{H\alpha 17}$	(7) CH $\alpha$	(8) $\frac{CH\alpha}{C30}$
NGC 4064	-12.31	40	25	25	-12.33	0.97	2.26
NGC 4178	-11.67	143	120	119	-11.69	0.15	0.60
NGC 4189	-11.92	71	58	63	-11.93	0.15	0.52
NGC 4192	-11.50	243	194	144	-11.61	0.17	0.50
NGC 4212	-11.77	71	55	63	-11.78	0.37	0.95
NGC 4237	-12.25	43	44	40	-12.25	0.55	1.17
NGC 4254	-10.95	168	123	142	-10.95	0.32	0.70
NGC 4293	-12.64	48	44	48	-12.64	1.00	2.50
NGC 4294	-11.79	69	51	60	-11.79	0.42	1.27
NGC 4298	-11.95	86	71	76	-11.96	0.45	1.25
NGC 4299	-11.70	40	28	39	-11.70	0.46	1.39
NGC 4303	-10.76	191	133	166	-10.76	0.49	0.96
NGC 4321	-11.13	228	148	159	-11.14	0.46	1.15
NGC 4351	-12.47	39	30	33	-12.48	0.77	2.08
NGC 4380	-12.64	72	63	33	-12.93	0.49	1.48
NGC 4383	-11.56	154	91	53	-11.62	0.84	1.33
NGC 4394	-12.25	100	89	59	-12.44	0.25	0.53
NGC 4405	-12.47	29	19	22	-12.48	0.91	1.94
NGC 4411B	-12.28	79	76	61	-12.33	0.35	1.09
NGC 4413	-12.31	39	34	39	-12.31	0.58	1.57
NGC 4419	-12.70	52	46	32	-12.83	0.64	1.23
NGC 4424	-12.22	40	27	32	-12.23	1.00	2.38
NGC 4429	-13.15	...	...	...	...	...	...
NGC 4438	-11.77	...	...	...	...	...	...
NGC 4450	-12.30	111	92	61	-12.38	0.69	1.41
IC 3392	-12.60	40	30	25	-12.63	0.82	2.22
NGC 4457	-11.91	38	33	...	-11.91	1.00	1.52
NGC 4459	-12.32	...	...	...	...	...	...
NGC 4498	-12.06	90	70	71	-12.08	0.25	0.81
NGC 4501	-11.21	140	112	132	-11.21	0.44	1.02
NGC 4519	-11.75	109	86	75	-11.79	0.14	0.41
NGC 4522	-12.39	149	54	43	-12.43	0.56	2.00
NGC 4527	-11.35	172	138	128	-11.38	0.29	0.69
NGC 4532	-11.40	119	68	72	-11.41	0.82	2.10
NGC 4535	-11.21	186	156	168	-11.22	0.17	0.59
NGC 4536	-11.42	256	198	134	-11.51	0.46	1.28
NGC 4548	-11.96	141	126	107	-12.06	0.11	0.26
NGC 4561	-12.11	42	34	40	-12.11	0.30	0.77
NGC 4567	-11.91	59	41	54	-11.91	0.55	1.10
NGC 4568	-11.59	99	72	79	-11.60	0.62	1.41

TABLE 7—*Continued*

(1)	(2)	(3)	(4)	(5)	(6)	(7)	(8)
Name	$\log F_{H\alpha}$	$r_{HII}$ (")	$r_{H\alpha 95}$ (")	$r_{H\alpha 17}$ (")	$\log F_{H\alpha 17}$	$CH\alpha$	$\frac{CH\alpha}{C30}$
NGC 4569	-11.83	72	65	72	-11.83	0.92	2.14
NGC 4571	-11.97	109	92	86	-12.01	0.27	0.79
NGC 4579	-11.54	108	90	99	-11.55	0.61	1.17
NGC 4580	-12.57	28	23	26	-12.58	0.93	2.27
NGC 4606	-12.67	50	47	28	-12.86	0.57	1.90
NGC 4639	-11.94	82	67	70	-11.95	0.25	0.50
NGC 4643	-12.30	...	...	...	...	...	...
NGC 4647	-11.72	80	57	62	-11.73	0.44	1.10
NGC 4651	-11.51	144	92	101	-11.53	0.56	1.02
NGC 4654	-11.60	176	101	92	-11.62	0.30	0.83
NGC 4689	-11.92	81	64	70	-11.93	0.67	1.76
NGC 4694	-12.87	30	25	20	-12.92	0.95	1.53
NGC 4698	-12.28	267	247	22	-13.24	0.31	0.61
NGC 4713	-11.62	101	63	72	-11.63	0.28	0.80
NGC 4772	-12.36	79	72	57	-12.47	0.43	0.84
NGC 4808	-11.71	129	65	67	-11.73	0.24	0.63

NOTE.— (1) Name of galaxy, (2) log of the total  $H\alpha$  flux in units of  $\text{erg cm}^{-2} \text{s}^{-1}$ , (3) radius in arcseconds of the outermost HII region, (4) radius in arcseconds which contains 95% of the total  $H\alpha$  flux, (5) radius in arcseconds at which the surface brightness falls to  $17 \times 10^{-18} \text{ erg cm}^{-2} \text{ s}^{-1} \text{ arcsec}^{-1}$ , (6) log of the  $H\alpha$  flux within  $r_{H\alpha 17}$  in units of  $\text{erg cm}^{-2} \text{ s}^{-1}$ , (7) the  $H\alpha$  concentration, and (8) the  $H\alpha$  concentration normalized by the central R concentration.

This figure "fig5a.jpg" is available in "jpg" format from:

<http://arxiv.org/ps/astro-ph/0106335v1>



This figure "fig5b.jpg" is available in "jpg" format from:

<http://arxiv.org/ps/astro-ph/0106335v1>

This figure "fig5c.jpg" is available in "jpg" format from:

<http://arxiv.org/ps/astro-ph/0106335v1>

This figure "fig5d.jpg" is available in "jpg" format from:

<http://arxiv.org/ps/astro-ph/0106335v1>

This figure "fig5e.jpg" is available in "jpg" format from:

<http://arxiv.org/ps/astro-ph/0106335v1>

This figure "fig5f.jpg" is available in "jpg" format from:

<http://arxiv.org/ps/astro-ph/0106335v1>

This figure "fig5g.jpg" is available in "jpg" format from:

<http://arxiv.org/ps/astro-ph/0106335v1>

This figure "fig5h.jpg" is available in "jpg" format from:

<http://arxiv.org/ps/astro-ph/0106335v1>

This figure "fig5i.jpg" is available in "jpg" format from:

<http://arxiv.org/ps/astro-ph/0106335v1>



This figure "fig5j.jpg" is available in "jpg" format from:

<http://arxiv.org/ps/astro-ph/0106335v1>

This figure "fig5k.jpg" is available in "jpg" format from:

<http://arxiv.org/ps/astro-ph/0106335v1>

This figure "fig5l.jpg" is available in "jpg" format from:

<http://arxiv.org/ps/astro-ph/0106335v1>

This figure "fig5m.jpg" is available in "jpg" format from:

<http://arxiv.org/ps/astro-ph/0106335v1>

This figure "fig5n.jpg" is available in "jpg" format from:

<http://arxiv.org/ps/astro-ph/0106335v1>

This figure "fig5o.jpg" is available in "jpg" format from:

<http://arxiv.org/ps/astro-ph/0106335v1>